A. P. Alexandrov
RESEARCH INSTITUTE
OF TECHNOLOGY
N I T I

Investigation of Corium Melt Interaction With NPP Reactor Vessel Steel (METCOR) Phase 2

PROGRESS REPORT

01/01/03 – 31/03/03

INVESTIGATION OF CORIUM MELT INTERACTION WITH REACTOR VESSEL STEEL IN NEUTRAL ABOVE-MELT ATMOSPHERE

MC-5 Test/03

Project title	Investigation of Corium Melt Interaction with NPP Reactor Vessel Steel (METCOR, Phase 2), No. 833.2
Ordered by	ISTC
File specification	METCOR2/PRMB-02
Project premises	The A.P. Alexandrov Research Institute of Technology (NITI) of the Russian Atomic Energy Ministry 188540, NITI, Sosnovy Bor, Leningrad Region, Russia
Project manager	Name V.B. Khabensky Signed
	Date May, 2003

Authors

Dr., Prof. V.B. Khabensky

Ph.D. S.V. Bechta

Ph.D. V.S. Granovsky

S.A. Vitol

E.V. Krushinov

Ph.D. S.Yu. Kotova

Dr., Corr.Mem.RAS V. V. Gusarov

Dr. Prof.. Yu. B. Petrov

Ph.D. I.V. Kulagin

Ph.D. D.B. Lopukh

Ph.D. A.Yu. Pechenkov

Ph.D. I.V. Poznyak

V.G. Bliznyuk

V.R. Bulygin

E.K. Kalyago

N.E. Kamensky

I.A. Loginov

A.V. Lysenko

V.I. Almjashev

A.P. Martynov

V.V. Martynov

E.V. Shevchenko

A.A. Chertkov

Summary

The Report offers a description and main findings from the MC-5 test in the framework of the ISTC METCOR, Phase 2 Project performed at NITI, Sosnovy Bor, on the Rasplav-3 test facility. The test results allowed evaluation of vessel steel oxidation kinetics at varying steel surface temperatures and heat fluxes from the molten C-100 corim to the steel specimen in argon atmosphere. The performed measurements and posttest analyses provide a basis for discussing the physico-chemical processes occurring at the interaction of molten corium and vessel steel through the corium crust.

CONTENTS

Introduction

In accordance with the work plan [1] and experimental matrix for the METCOR, Phase 2 Project, a series of tests has been performed on the interaction of fully oxidized C-100 corium and vessel steel through corium crust in the oxygen-free medium, i.e. under the conditions that predetermine the minimum chemical interaction of the melt and the steel specimen.

The oxygen-free above-melt atmosphere was modelled in tests by argon. The tests were set up as a research on the influence of the steel specimen surface temperature on its oxidation kinetics.

The MC-5 test employed a technique of on-line noncontact determination of the metal ablation rate by means of ultrasonic sounding of the steel specimen. The use of this technique made it possible to perform a series of tests within one melting session.

Experimental objective

The experimental objective was to study molten corium-vessel steel interaction kinetics at three different steel surface temperatures under the conditions determining the minimum chemical interaction (C-100 corium, inert atmosphere).

1. Test description

1.1. Equipment

The test employed a modernized facility featuring a high-frequency generator with 60 kW oscillating capacity and 0.13 MHz current frequency. The melt was prepared using the technique of induction melting in the cold crucible [2]. The furnace schematic diagram and appearance are shown in Figs.1.1.1, 1.1.2.

Top (12) and bottom (13) calorimeters were provided for cooling the specimen and determining heat fluxes to specimen (11) from the melt, as well as for cooling the specimen/ultrasonic sensor (15) contact area. To avoid the specimen induction heating, the crucible sections were welded together in their lower part to form an electromagnetic screen (18). The specimen was placed in the crucible in such a way that its top was 1 mm lower than the weld seam upper edge. The gap between the specimen and crucible sections was filled with powdered ZrO_2 (9) and fused ZrO_2 granules (10). Movable water-cooled electromagnetic screen (3) provided additional shielding of the specimen. The melt surface was monitored through the water-cooled pyrometer shaft blown through with argon (1).

A sketch and appearance of the specimen produced from 15Kh2NMFA-A vessel steel are given in Figs.1.1.3 and 1.1.4. Table 1.1.1 provides the layout of K-type thermocouple junctions in the specimen. Within a radius of 10 mm from the specimen axis, the thermocouples were placed in ∅ 1.5 mm channels, and within a radius of 29 mm – in milled grooves 1.5 mm wide.

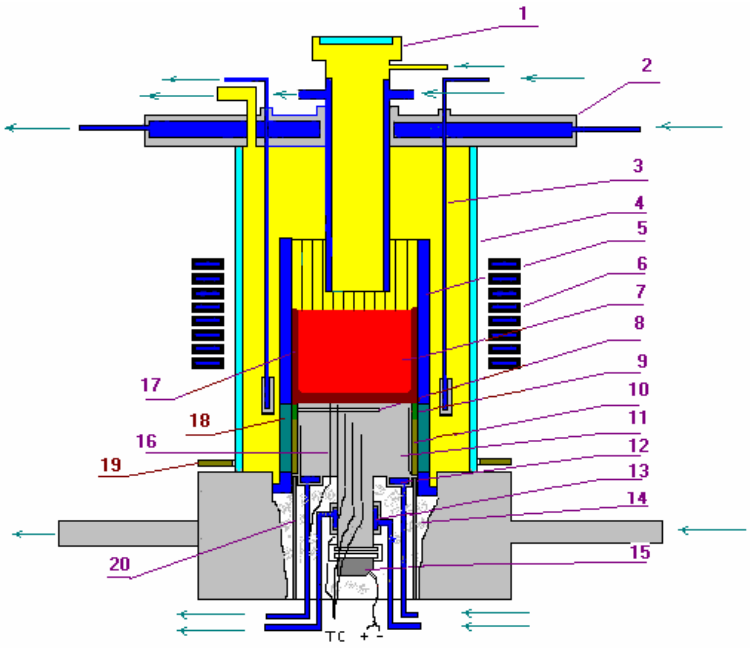

1 – water-cooled pyrometer shaft; 2 – water-cooled cover; 3 – water-cooled electromagnetic screen; 4 – quartz tube; 5 – crucible section; 6 – inductor; 7 – melt; 8 – acoustic defect; 9 – fused ZrO_2 granules thermal insulation; 10 – ZrO_2 powder thermal insulation; 11 – vessel steel specimen; 12 – specimen top calorimeter; 13 – specimen bottom calorimeter; 14 – kaolin wool thermal insulation; 15 – ultrasonic sensor; 16 – thermocouples; 17 – crust, 18 – electromagnetic screen; 19 – uncooled electromagnetic screen; 20 – specimen cylindrical support

Fig. 1.1.1. Furnace diagram

Fig. 1.1.2. Furnace appearance before the test

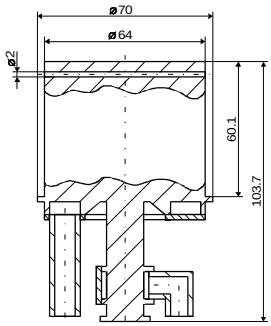

Fig. 1.1.3. Specimen sketch

Fig. 1.1.4. Specimen appearance

Table 1.1.1.

Thermocouple junctions layout in the vessel steel specimen

Thermocouple No.	TC 01	TC 02	TC 03	TC 04	TC 05	TC 06	TC 07	TC 08	TC 09	TC 10	TC 11	TC 12	TC 13
Angle, α, deg.	0	270	180	225	90	315	45	135	270	180	45	315	45
Distance from specimen axis to junction, r, mm	10.0	10.0	10.0	10.0	10.0	10.0	10.0	29.0	29.0	29.0	29.0	29.0	7.5
Distance from specimen top to junction, h, mm	0.0	2.0	4.0	6.0	6.0	8.0	20.0	0.0	2.0	4.0	20.0	40.0	101.7

To use the technique of noncontact control of the vessel steel corrosion rate, acoustic defect (8) was made in the steel specimen (Fig.1.1.1.). Optimization of the ultrasonic converter (15) resonance frequency made it possible to select its working frequency at 2.5 MHz. The performed

modernization of the ultrasonic measurement technique allowed real-time monitoring of the specimen length change vs. its temperature change.

Air-tightness of the furnace was ensured by quartz tube (4) and water-cooled cover (2).

To control oxygen partial pressure in the gas removed from the furnace and for making up mass balance for the test, a system of gas supply and removal was used (Fig. 1.1.5.). Oxygen partial pressure in the removed gas was measured by electrochemical sensor (12).

Large area filters (9), switched in turn, were used for purifying the gas from aerosols. Such gas flow parameters as consumption and pressure were controlled at the points indicated in the diagram by the electromechanical flowmeters G1 and G2 of OR-40/S type, G3 rotameter and P1-P4 pressure gauges of 'Corund-DIV' type. Silica gel column (2) was installed at the gas circuit inlet to the furnace for removing traces of moisture from the gas. Argon was supplied from cylinder (1) via shaft (4), thus ensuring a higher quality of both pyrometric measurements and video recording by blowing aerosols away.

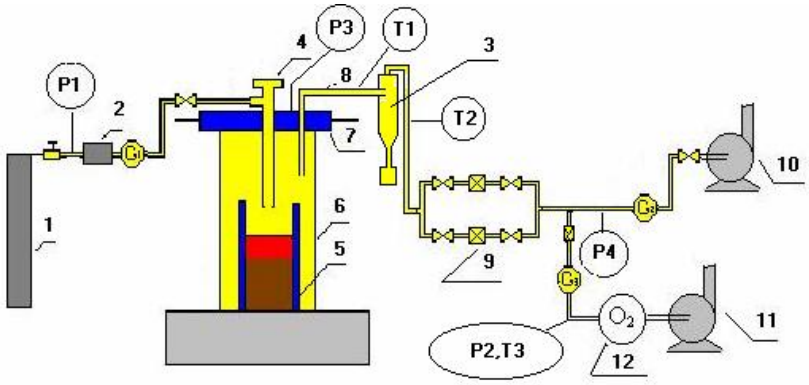

1 – argon cylinder; 2 – silica gel dryer; 3 – cyclone separator; 4 – pyrometer shaft; 5 – crucible; 6 – quartz tube; 7 – water-cooled cover; 8 – aerosol trunk line; 9 – large area filters; 10 – fan; 11 – vacuum pump; 12 – oxygen sensor; P1-P4 – pressure gauges; G1, G2 – flowmeters; G3– rotameter; T1–T3 – thermocouples

Fig.1.1.5. Gas supply and removal system

The crucible was loaded with charge in argon using a special procedure. At first, a 5-mm layer of C-100 corium (70 UO_2 - 30 ZrO_2, mass %, here and further in text) was placed on the specimen top. Particles dispersion did not exceed 50 μm. Then followed a C-100 corium layer with 200-1000 μm particles dispersion. This layer was covered with a mixture of UO_2 and ZrO_2 powders taken in the 70% / 30% ratio.

C-100 corium had been previously fused in argon in a separate Pr2-MC5 test.

The charge start-up heating was was done using 1.5 g of metallic zirconium.

1.2. Materials

The materials used in the test included 15Kh2NMFA-A vessel steel, urania, zirconia, metallic zirconium, and high-purity argon. All materials have been checked for the main substance content. In addition, the powdered urania was checked by thermogravimetry and the oxygen/uranium ratio was found to equal 2.0. Table 1.2.1. shows the corium charge composition. The composition and masses of substances loaded into the crucible before melting are given in Tab. 1.2.2.

Table 1.2.1.

Corium charge composition

Component	Main substance content, %	Impurities, %	Note
UO_2	> 99.0	Fe < 0.03; As < 0.0003; Cu < 0.01; phosphates < 0.002; chlorides < 0.003	Passport data; Thermogravimetry
ZrO_2	(ZrO_2+ HfO_2) > 99.3	Al_2O_3<0.03; Fe_2O_3<0.05; CaO<0.03; MgO<0.02; SiO_2<0.2; TiO_2<0.1; P_2O_5<0.15; (Na_2O+K_2O)<0.02	Passport data
Zr	H-1 alloy	Nb<1.0	XRF

Table 1.2.2.

Composition and masses of substances loaded into the crucible before melting

Purpose	Component	Fraction, μm	Mass, g	mass %
Main charge	Fused corium C-100 (70%UO_2 – 30% ZrO_2)	< 50	101.2	5.6
		200 – 1000	299.7	16.7
	Urania, UO_2	< 50	1013.3	56.5
	Zirconia, ZrO_2	< 50	365.4	20.4
Start-up material	Metallic zirconium, Zr	Rods 3 mm in diameter and 15 mm high	15.1	0.8
		Total	1794.7	100

The required fractions of urania and corium were achieved in argon atmosphere by crushing the pellets from fuel rods and the C-100 corium ingot previously fused in Pr2-MC5 test, respectively. An average sample of the crushed ingot was subjected to XRF and spectrophotometry.

For creating the oxygen-free above-melt atmosphere, argon of high purity grade was used.

1.3. Experimental procedure

To prevent a possible heating of the specimen during the start-up melting, its top was positioned at a distance of 40 mm from the inductor bottom ring, and the top of movable electromagnetic screen was positioned level with the inductor bottom. The charge start-up heating was performed in argon, and the specimen top temperature was controlled using thermocouple readings. When producing the molten pool, some actions were taken to optimize the position of both the crucible and movable electromagnetic screen relative to the inductor (see Figs. 1.3.1-1.3.3):

- 913 sec. Electromagnetic screen shifted 10 mm downwards.
- 1,198 sec. Crucible introduced into inductor for 10 mm (according to the design, the screen moves together with the crucible).
- 1,298 sec. Screen shifted 10 mm downwards.
- 1,398 sec. Argon fed into the furnace at 600 l/h.
- 1,578 sec. Crucible shifted 3 mm downwards.

- 2,598 sec. Crucible shifted 3 mm upwards.
- 3,278 sec. Crucible shifted 5 mm upwards.
- 3,378 sec. Screen shifted 3 mm downwards.
- 3,538 sec. Screen shifted 3 mm downwards.
- 3,988 sec. Screen shifted 2 mm downwards.

As a result, the molten pool on the specimen was formed in such a way that its top was 25 mm below the inductor and 10 mm below the movable electromagnetic screen top. Further on, the crucible and screen were not moved and stabilization of temperature values at the specimen top was achieved by changing the power source operating mode.

In accordance with the experimental plan, melt samples were taken, pool depth and bottom crust thickness were measured during each period of stabilized temperature at the specimen top. The samples were subjected to rapid analysis of the main components content, and the compsition and mass of the correcting addition to be introduced into the melt was determined.

Throughout the test, the melt temperature was permanently measured through the water-cooled shaft blown with argon (Fig. 1.3.1.) by the RAYTEK spectral ratio pyrometer of MR1SCSF series with wavelengths of 0.75–1.1 μm – 0.95–1.1 μm. Periodically the melt surface was recorded on video.

At 4,638 sec the melt was sampled and the pool depth and bottom crust thickness were found to be 56 and 3 mm, respectively. Then the interaction of molten corium and specimen was provided in the conditions of the specimen top temperature stabilized at ~ 1000°C (see Fig. 1.3.2.) for 5 hours. The TC01 thermocouple readings (Fig. 1.3.2.) are excessive, presumably due to location of the junction within the crust at the specimen surface. According to the on-line echogram processing, no corrosion of the specimen was recorded. At 22,516 sec, melt sampling was repeated and the pool depth and bottom crust thickness were found to be 59 and 3 mm, respectively. An increase in pool depth was presumably due to the collapse into the melt and meltdown of crusts from the crucible section inner surfaces, it being indirectly confirmed by the redistribution of heat fluxes into the furnace components (Fig. 1.3.3.). At 22,663 sec, a corrective addition of 85 g of urania was introduced into the melt. Upon its dissolution, the melt was sampled again.

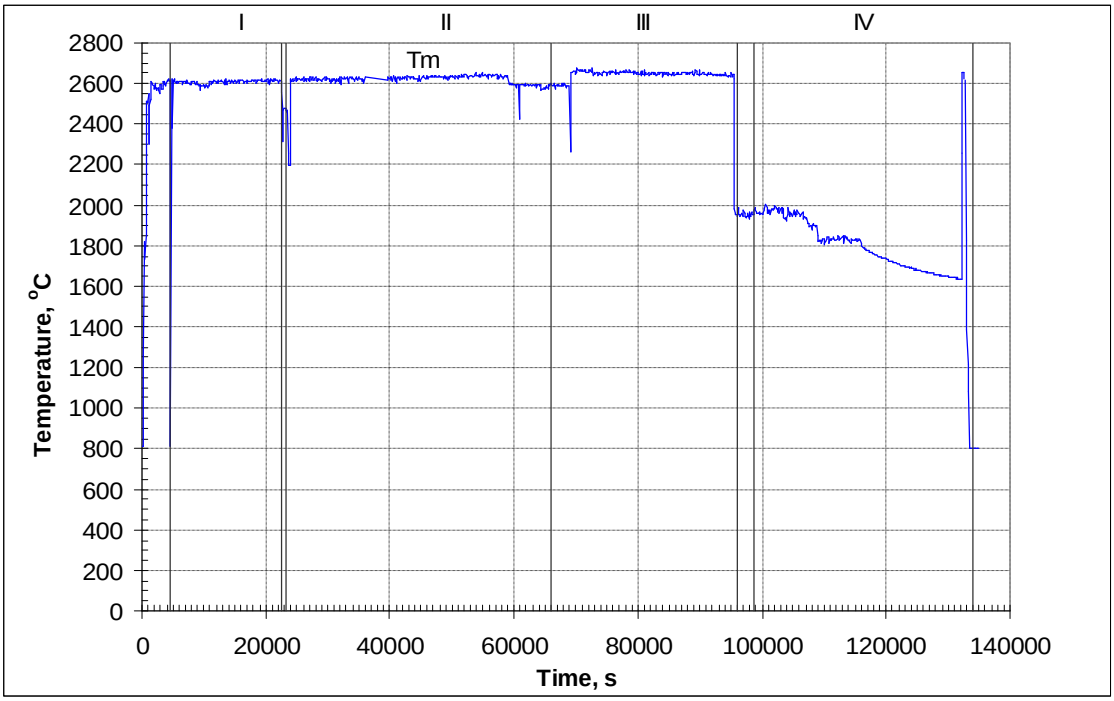

Fig. 1.3.1. Pyrometer readings in the test

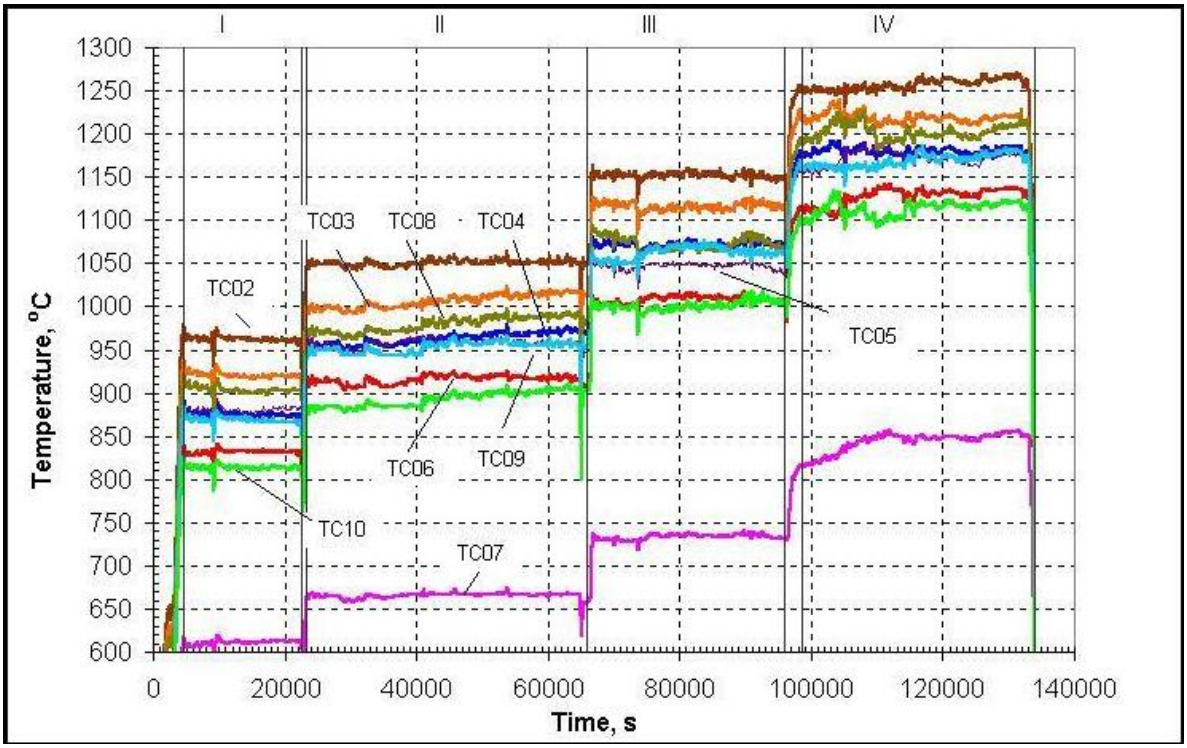

Fig. 1.3.2. Thermocouple readings in the test

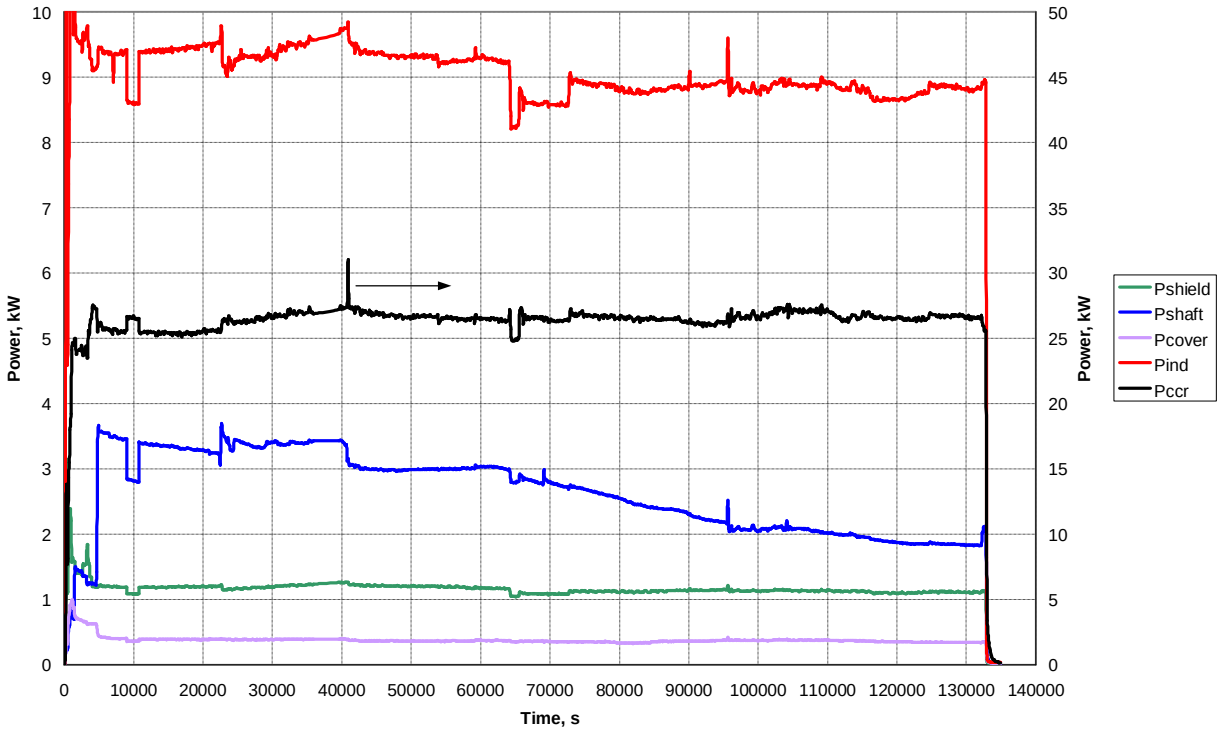

P_{ccr} –power extracted from cold crucible by cooling water; P_{ind} –; power extracted from inductor coil by cooling water; P_{shaft} –power extracted from shaft by cooling water; P_{screen}– power extracted from electromagnetic screen by cooling water; P_{cov} – power extracted from furnace lid by cooling water

Fig. 1.3.3. Heat and electromagnetic fluxes history in the test

By regulating the power source operating mode, the power in the melt was increased and starting from 23,250 sec the interaction of melt and vessel steel specimen was provided for 11 hours under the conditions of stabilizing the temperature on the specimen top at ~ 1100ºC. At 40,900 sec a stepwise increase of heat fluxes into the crucible was observed which, to our opinion, is related to the collapse into the melt of aerosol sediments from the crucible sections where they accumulate as uranium oxide keeps evaporating from molten corium. A considerable evaporation of UO_2 led by 53,100 sec to clogging of the aerosol removal line which was cleaned after switching over to the spare one. According to the on-line echogram processing, the specimen corrosion depth amounted to 0.07 mm for 11 hours.

At 60,303 sec the melt was sampled and the pool depth and bottom crust thickness were found to be 60 and 2.8 mm, respectively. At 64,350 sec, a corrective addition of 83 g of urania was introduced into the melt. By regulating the power source operating mode, the temperature on the specimen top was stabilized at ~ 1200ºC and maintained for 8.5 hours. At 70,205 sec and 91,052 sec the melt was sampled and the pool depth and bottom crust thickness measured. In the first case, the pool was 62 mm deep and the crust was 3 mm thick. In the second case, the pool was 64 mm deep and the crust was 2.8 mm thick. According to the on-line echogram processing, the specimen corrosion depth was 0.1 mm for 8.5 hours.

At 95,000 sec the accretions that had formed on the crucible sections owing to the melt vapours condensation were knocked down into the melt. This led to formation of a massive crust on the melt surface. By regulating the power source operation mode, the temperature on the specimen top was stabilized at 1300ºC and the interaction of melt and vessel steel specimen was provided for 10 hours at this last steady-state level. At 132,570 sec the crust was broken and it became possible to measure the molten pool depth and crust thickness which appeared to be 58 and 2.5 mm, respectively. The hole in the crust was used for measuring the temperature in the melt/crust area with a tungsten sheathed W/Re thermocouple (see Fig. 1.3.4.).

According to the echogram processing, the depth of corrosion amounted to 0.1 mm for 10 hours. At the same time, however, the echogram readings were anomalous and showed a reduction of the corrosion depth within a separate time interval.

At 133,120 sec induction heating was disconnected. Crystallization of the melt and cooling of the corium ingot were carried out in argon. Apperanace of the furnace after the test is given in Fig. 1.3.5. Appearances of products from the melting and of the steel specimen are shown in Figs. 1.3.6 and 1.3.7.

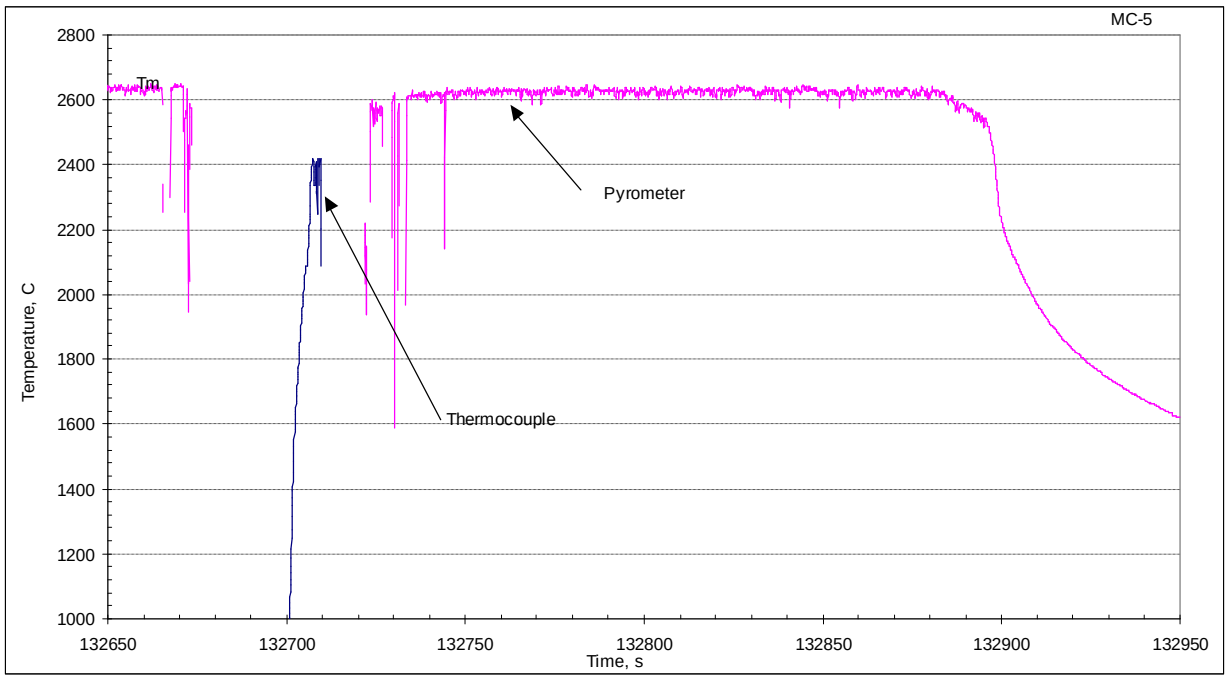

Fig. 1.3.4. Immersible thermocouple and pyrometer readings

Fig. 1.3.5. Appearance of the furnace after the test

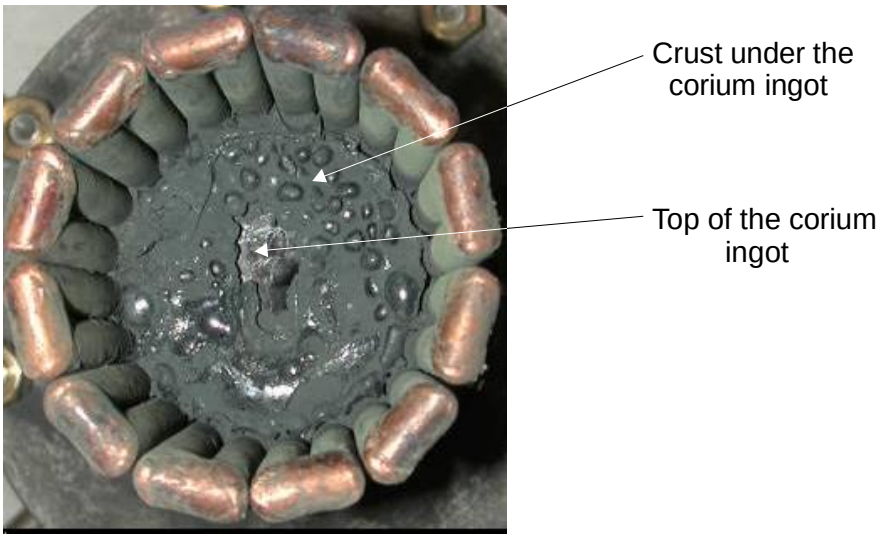

Fig. 1.3.6. Corium ingot in the cold crucible

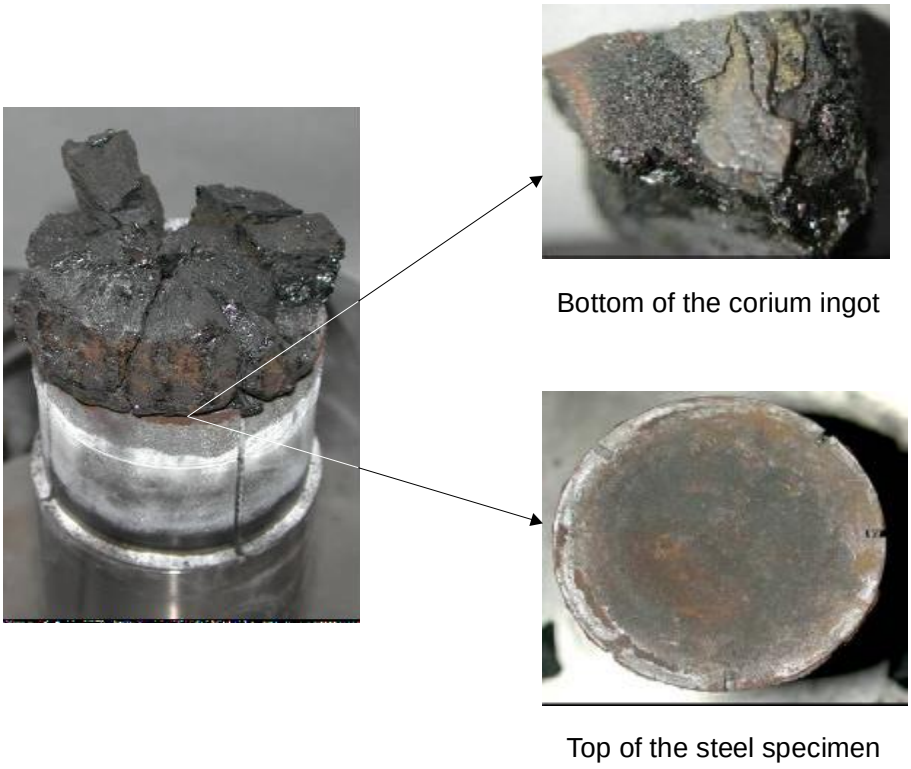

Fig. 1.3.7.. Corium – specimen view after crucible is disassembled.

1.4. Correction of the melt composition in the test

Correction of the molten corium composition was made in order to prevent the uranium oxide depletion. The corium composition was judged by the results of rapid analysis of melt samples taken and cooled in argon. The results of XRF rapid analysis of corium samples are presented in Tab. 1.4.1. The corrective additions to the melt were introduced as standard urania pellets.

Table 1.4.1.

Results of corium samples rapid analysis

Sample No.	U	Zr	O*
1	62.1	21.8	16.0
2	61.1	21.2	17.7
3	64.3	20.0	15.7
4	60.8	22.9	16.2
5	65.7	18.9	15.5
6	64.8	19.6	15.6
7	64.5	19.3	15.8

* - determined from the residue.

The results of posttest refined XRF analysis of oxidic corium samples are given in Tab. 1.4.2.

Table 1.4.2.

Results of refined XRF analysis of corium samples

Element	Sample No.						
	1	2	3	4	5	6	7
U	63.6	62.0	63.9	62.7	64.4	63.9	64.5
Zr	20.3	21.6	19.7	20.8	19.5	19.7	19.3
Fe	0.2	0.2	0.5	0.3	0.2	0.5	0.4
O*	15.9	16.2	15.9	16.2	15.9	15.9	15.8

* - determined from the residue.

Fig. 1.4.1 shows the changes in equilibrium concentrations of uranium, zirconium and oxygen in the melt during the test (based on the results of the refined XRF analysis).

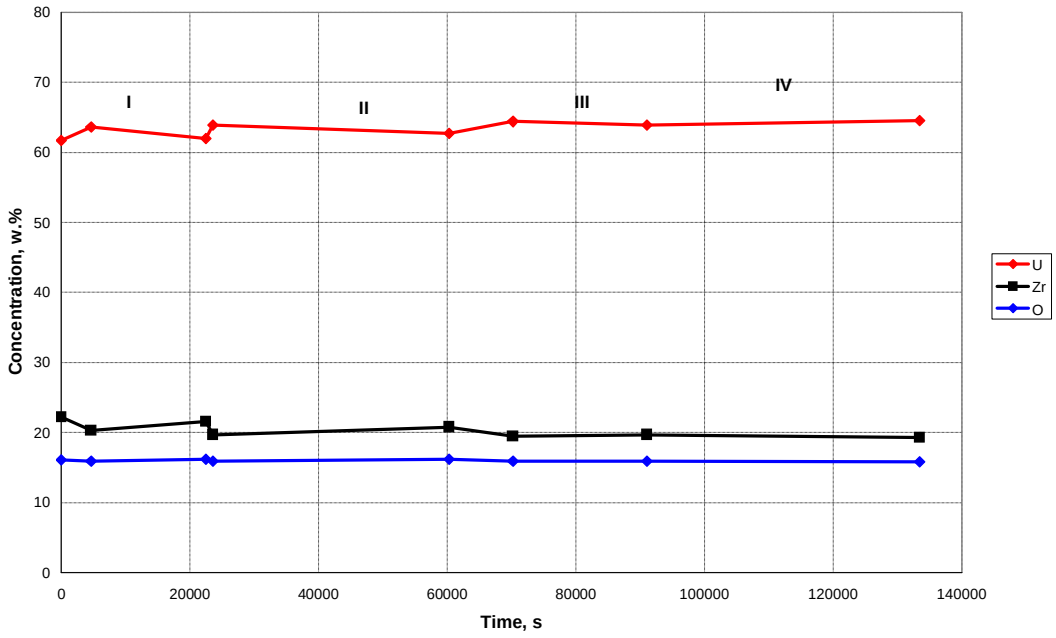

Fig.1.4.1. Changes in equilibrium concentrations of uranium, zirconium and oxygen in the melt during the test

2. Posttest analysis

2.1. Numeric modelling of the specimen temperature conditions

In order to determine the temperature and heat flux density at the upper top of the specimen for four steady-state regimes, calculations of the specimen temperature conditions have been performed. In the calculations a finite-element programme was used, which applied the solution of a stationary heat conductivity equation in the axis-symmetrical formulation. Boundary conditions were fixed as the temperature on the inner surface of the top calorimeter (see Figs 1.1.3. and 1.1.4.) estimated at 100°C (calculation results are practically insensitive to the insignificant error of its determination), the temperature on the inner surface of the bottom calorimeter (20°C) and the temperature on the outside surface of peripheral thermal insulation layer (see Fig. 1.1.1.) accepted as equal to the average temperature of cooling water. Thermal conductivity of 15Kh2NMFA-A steel, from which the specimen was produced, was taken from the results of the ISTC METCOR, Phase 1 Project [3]. In the calculations, the heat flux density into the specimen top and the heat conductivity of the insulating layer were varied to provide the best agreement between calculated and measured specimen temperatures at the locations of thermocouple junctions. Using the Pr1-MC6 results, the radial distribution of density of the heat flux into the specimen top was determined. The obtained distribution values were roughly taken into consideration in the performed calculations.

The results of calculations for the four steady-state regimes are given in Figs. 2.1.1-2.1.4 and in Tab. 2.1.1. Figs. 2.1.1 a) – 2.1.4 a) present the measured and calculated temperatures of the specimen 10 and 29 mm off the specimen axis. Their comparison shows the results of calculations and measurements to be in satisfactory accord. Figs. 2.1.1 b) – 2.1.4 b) show the calculated radial temperature distribution across the specimen top. Figs. 2.1.1 c) – 2.1.4 c) give the calculated temperature distribution along the specimen axial section. Table 2.1.1. gives the calculated heat flux densities to the specimen top (average ones and those in the centre of the ultrasonic sensor ∅15 mm sighting spot), maximum temperatures in the centre of the specimen top, as well as the calculated and measured power into the top calorimeter (the power into the bottom calorimeter is negligibly small).

Table 2.1.1.

Calculated and measured power, heat flux and temperature

Regime	Heat flux density, average, MW/m^2	Heat flux density, ∅ 15 , MW/m^2	Power into the top calorimeter, calculated, kW	Power into the top calorimeter, measured, KW	Maximum temperature, °C
1	0.66	0.95	1.28	1.40	1073
2	0.73	1.05	1.42	1.46	1180
3	0.81	1.20	1.60	1.58	1315
4	0.89	1.30	1.75	1.75	1434

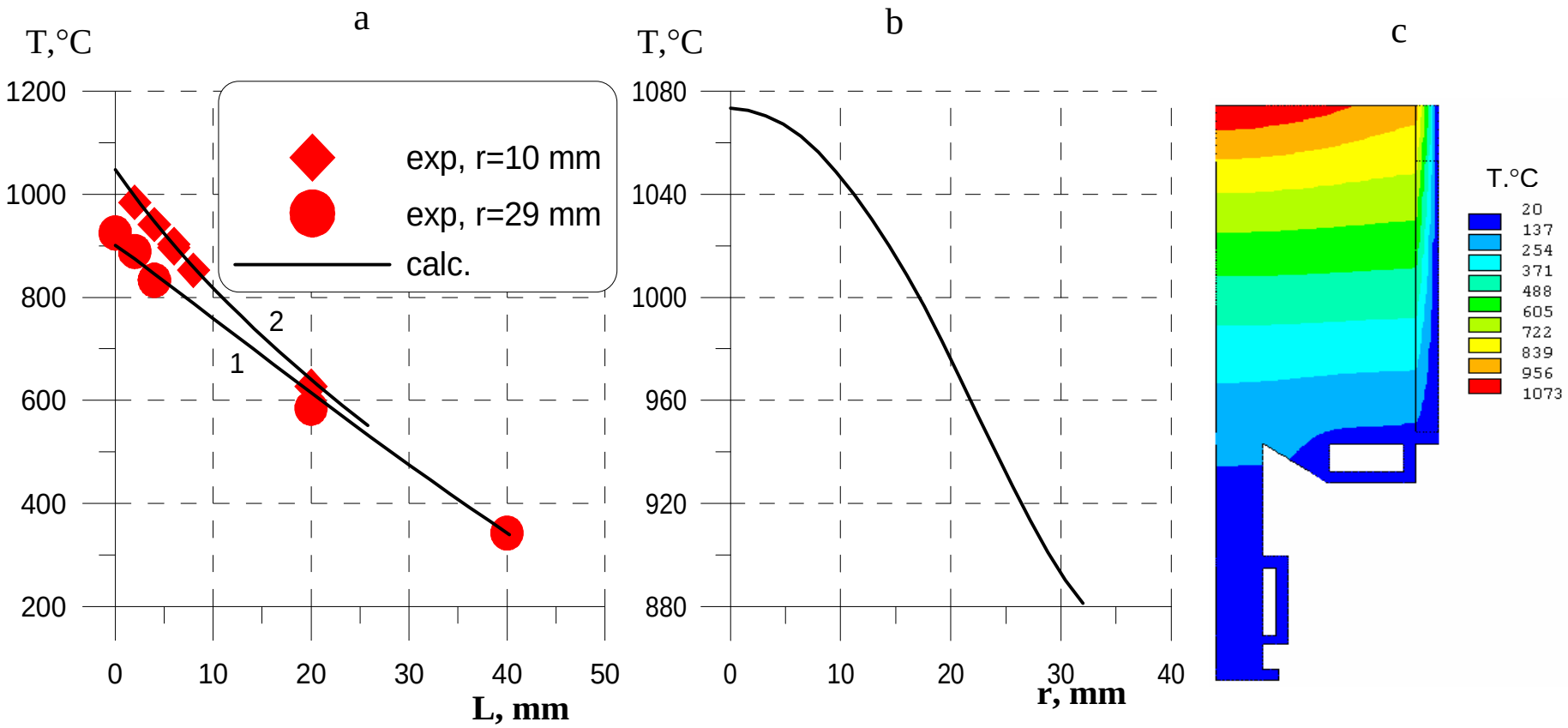

a – axial distribution of temperatures; b – radial distribution of temperatures across the specimen upper surface; c – temperature field in the specimen (and in the insulation)

Fig. 2.1.1 Calculated temperature distribution in the specimen (4,600-22,500 sec)

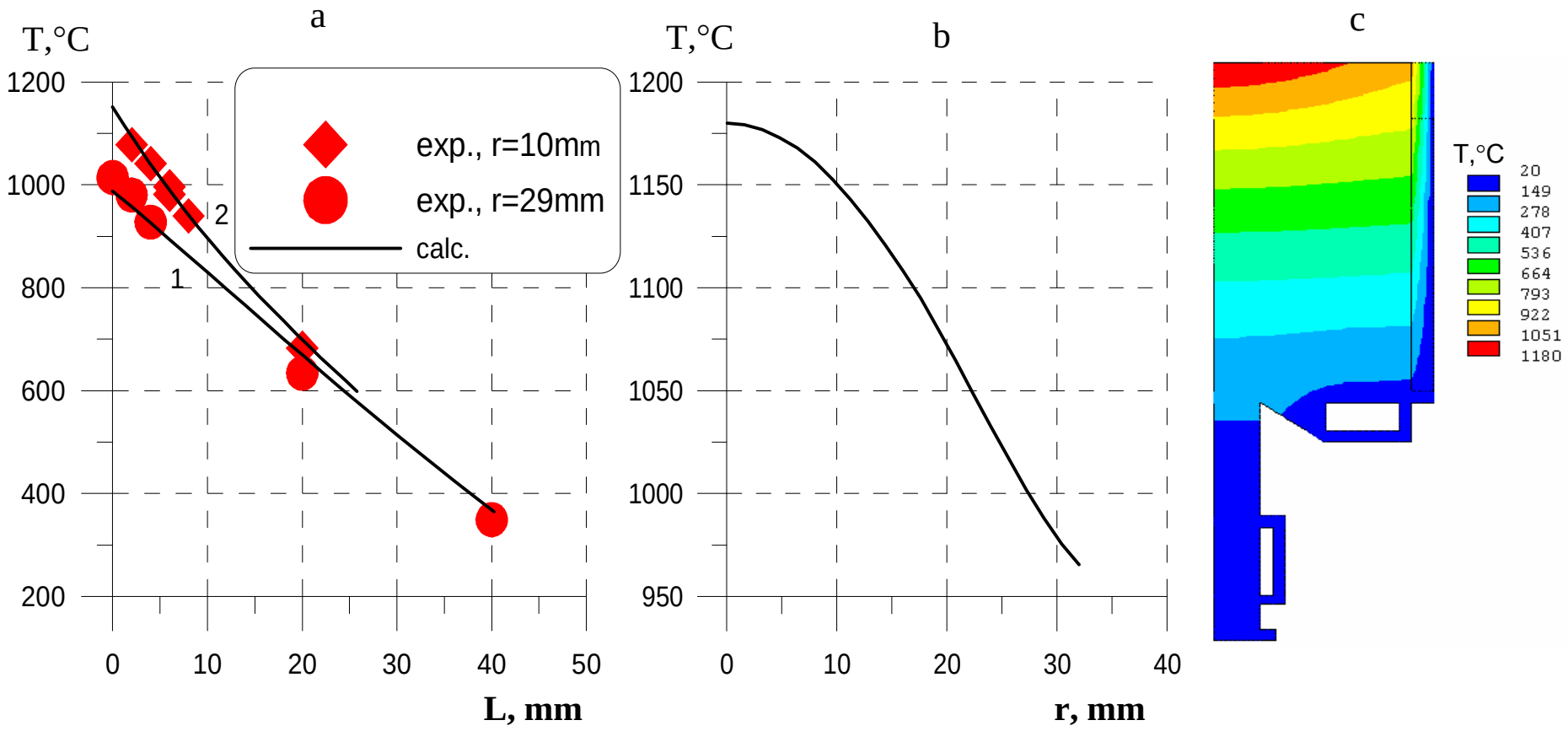

a – axial distribution of temperatures; b – radial distribution of temperatures across the specimen upper surface; c – temperature field in the specimen (and in the insulation)

Fig. 2.1.2 Calculated temperature distribution in the specimen (23,200-60,300сек)

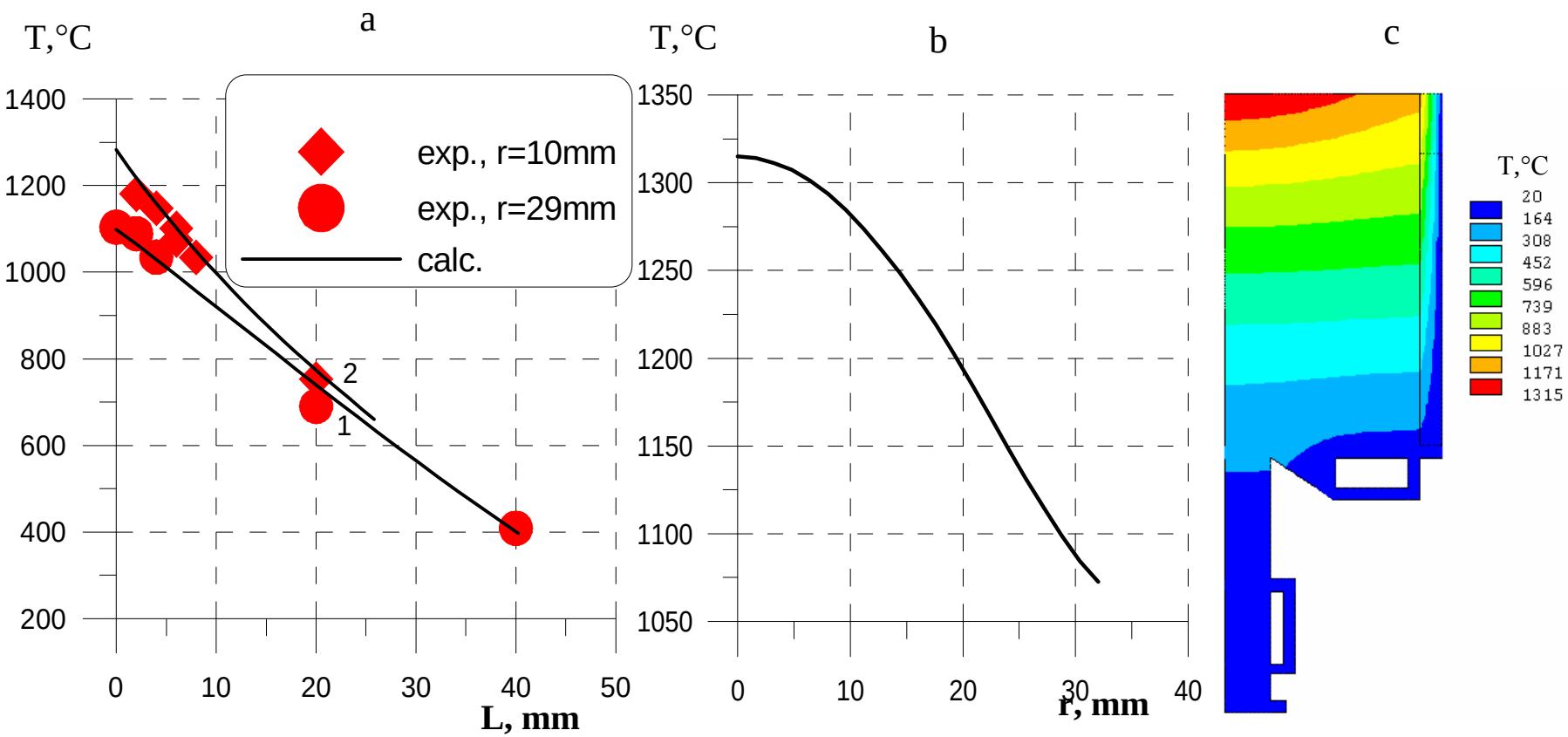

a – axial distribution of temperatures; b – radial distribution of temperatures across the specimen upper surface; c – temperature field in the specimen (and in the insulation)

Fig. 2.1.3 Calculated temperature distribution in the specimen (65,900-96,000 sec)

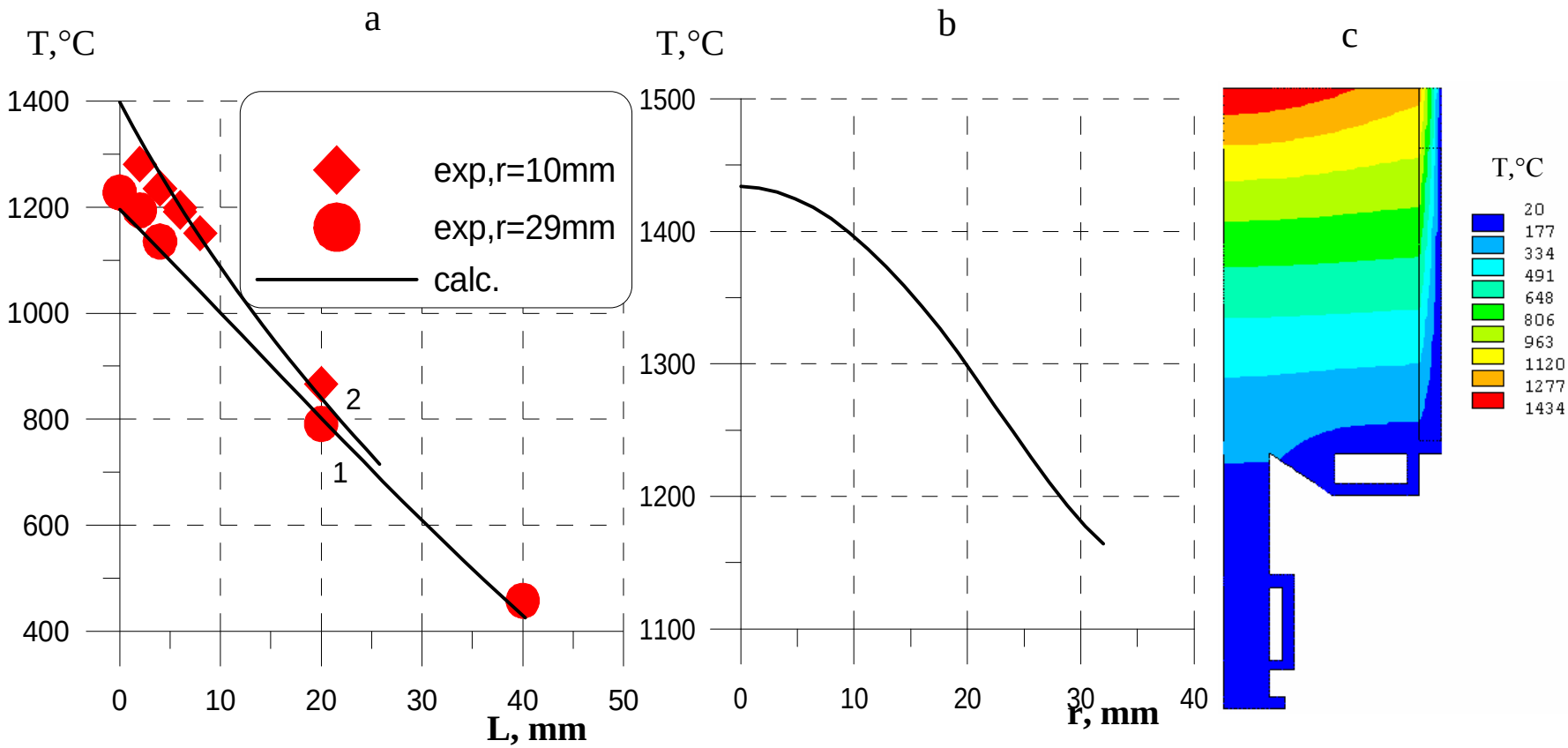

a – axial distribution of temperatures; b – radial distribution of temperatures across the specimen upper surface; c – temperature field in the specimen (and in the insulation)

Fig. 2.1.4 Calculated temperature distribution in the specimen (98,500-133,900 sec)

2.2. Calculation of electromagnetic parameters of the induction system

Fig. 2.2.1 shows a sketch of the electromagnetic system which includes the inductor, the cold crucible with sections and manifold, the vessel steel specimen, molten corium, the furnace cover, electromagnetic screens and the pyrometer shaft.

The solution of an electromagnetic problem yields integral parameters of the induction system, distributions of heat sources and Lorentz forces in molten corium, and distribution of heat sources on the specimen.

Since reliable data on the specific electrical resistance of corium with the composition in question are absent, an inverse problem was solved. One of its arguments was the value of specific resistance averaged for the molten corium volume. To ensure determination or overdetermination of the system, the other input parameters were the inductor voltage and power, total power in the melt and cold crucible. Thus, solving of the inverse problem was based on the minimization of the functional, in which the parameter function is the electromagnetic field equation allowing for the accepted limitations and input parameters, and the the equation below:

$$Q_{ccr} + Q_{cov} + Q_{sh} + Q_{sp} = Q_{spe} + Q_{ccre} + Q_{melt} + Q_{cove} + Q_{she},$$

where Q_{ccr} is the total power removed from the crucible; Q_{cov} - the total power removed from the cover; Q_{sh} - the total power removed from the shaft; Q_{sp} - the total power removed from the specimen; Q_{spe} – the power induced in the specimen; Q_{ccre} - the power induced in the crucible; Q_{melt} is the power in the melt; Q_{cove} - the power induced in the cover, and Q_{she} - the power induced in the shaft.

Numeric calculations were performed using the programme described in [4].

Table 2.2.1 summarizes the measured and calculated data for the four stages of the test, which correspond to different temperature conditions of the specimen, where a_2 is the molten pool depth, ξ is the bottom crust thickness and ρ_2 is the average volumetric specific electrical resistance.

The finite-element grid for the molten pool and the vessel steel specimen, as well as the distribution of power and Lorentz forces in the molten corium pool for the four temperature conditions of the specimen are shown in Figs. 2.2.2 - 2.2.18.

Similar values of the specific electrical resistance of the melt obtained for all the four regimes confirm reliability of the calculation method. The distribution of power in the specimen, shown in the figure, suggest that the direct specimen heating by the electromagnetic field occurs in a small area of the surface layer. The total power of this heat does not exceed 40 W, it being less than 2% of the power from the melt to the specimen.

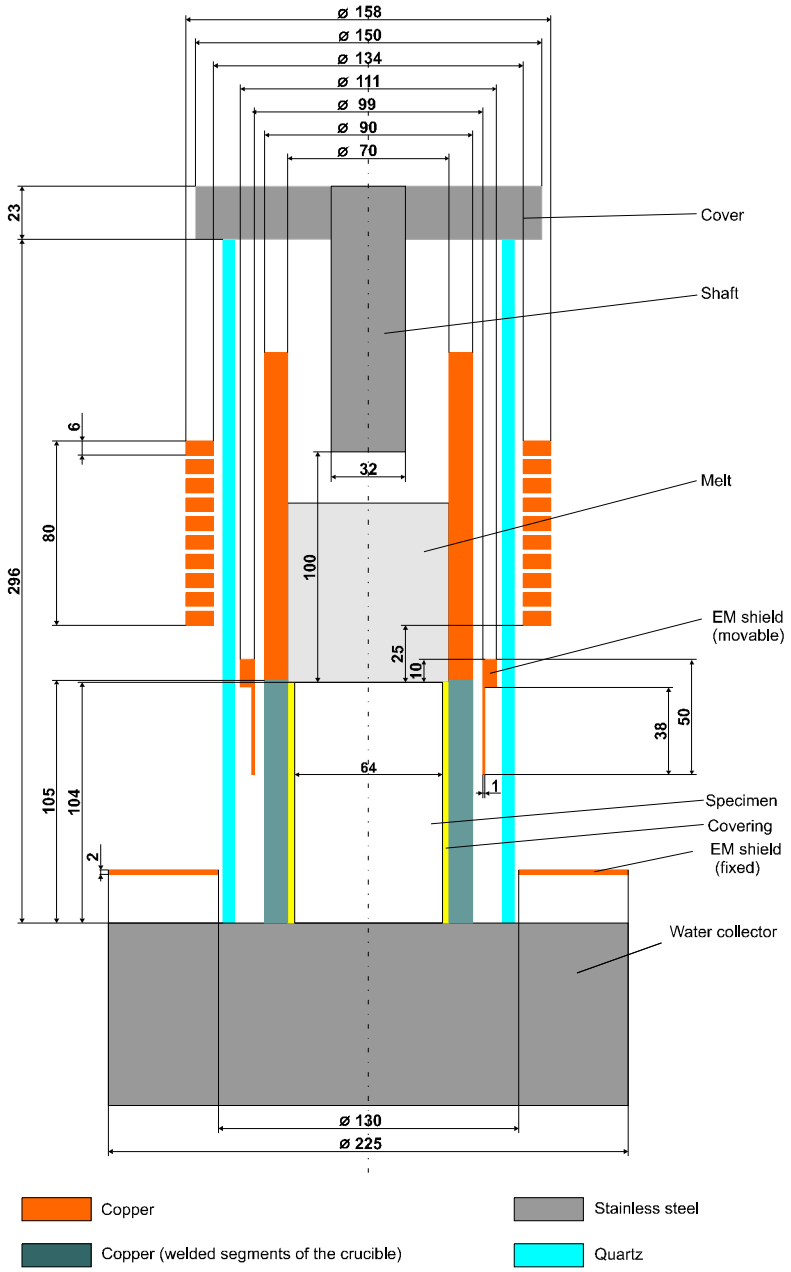

Fig. 2.2.1. Electromagnetic system sketch

Table 2.2.1.

Actual test experimental and calculated data

Time, Sec	a_2, mm	ξ, mm	Q_{sp}, KW	Q_{ccr}, kW	Q_{cov}, KW	Q_{sh}, kW	Q_{spe}, kW	Q_{ccre}, kW	Q_{melt}, KW	Q_{cove}, kW	Q_{she}, kW	ρ_2, Ohm·cm
	Experimental						Calculated					
22615	59	3.0	1.46	25.6	0.4	3.3	0.04	9.5	20.16	0.11	0.95	0.024
60303	60	2.75	1.52	26.7	0.4	2.9	0.03	8.5	21.98	0.10	0.91	0.023
91052	64	2.75	1.65	26.4	0.3	2.3	0.03	8.1	21.55	0.10	0.87	0.027
132811	58	2.75	1.83	26.5	0.3	1.8	0.03	7.9	21.31	0.09	1.1	0.022

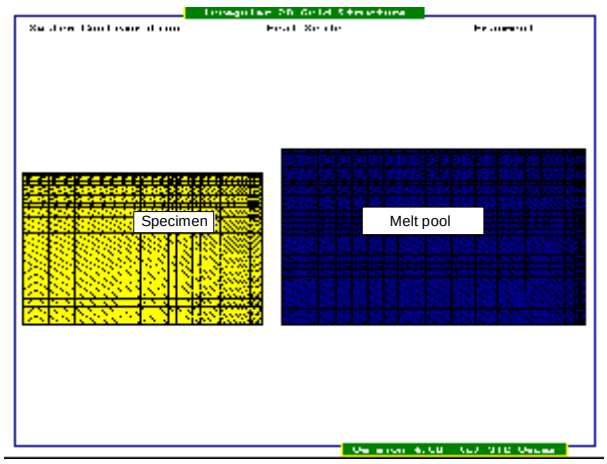

Fig. 2.2.2. Finite-element grid of the calculated regions

The first temperature condition of the specimen (22,500 sec)

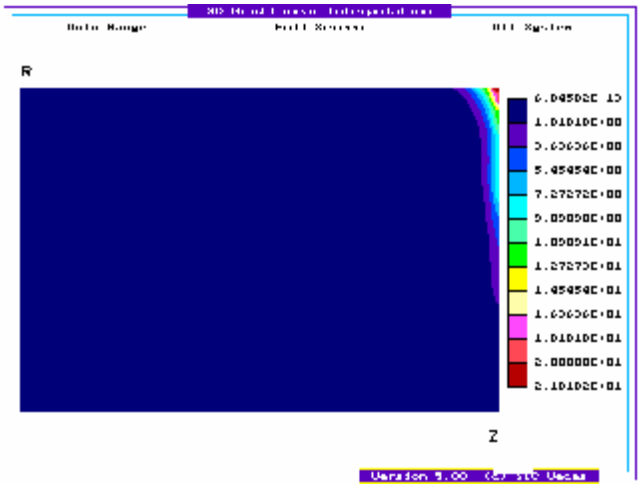

Fig. 2.2.3. Distribution of power in the specimen, W/cm^3

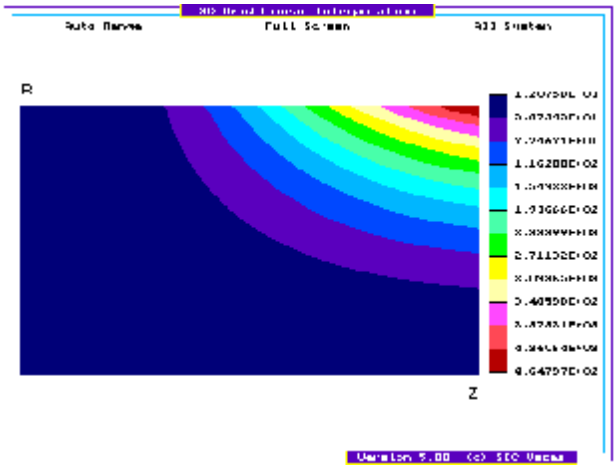

Fig. 2.2.4. Distribution of power in the melt, W/cm^3

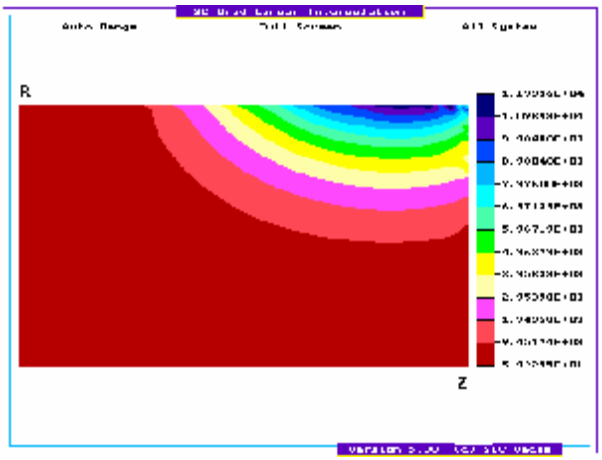

Fig. 2.2.5. Distribution of Lorentz forces in the melt (radial vector component), N/cm^3

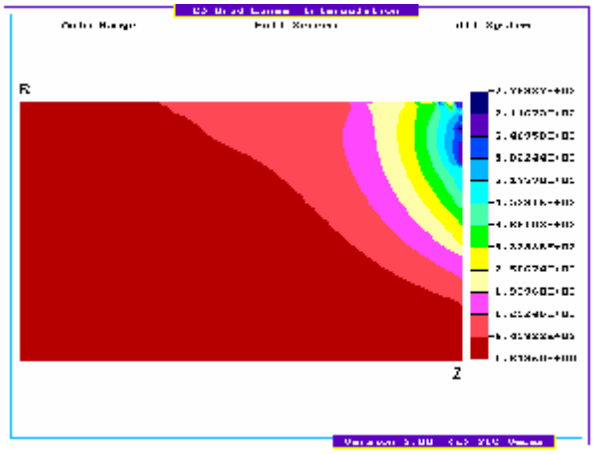

Fig. 2.2.6. Distribution of Lorentz forces in the melt (axial vector component), N/cm^3

The second temperature condition of the specimen (60,300 sec)

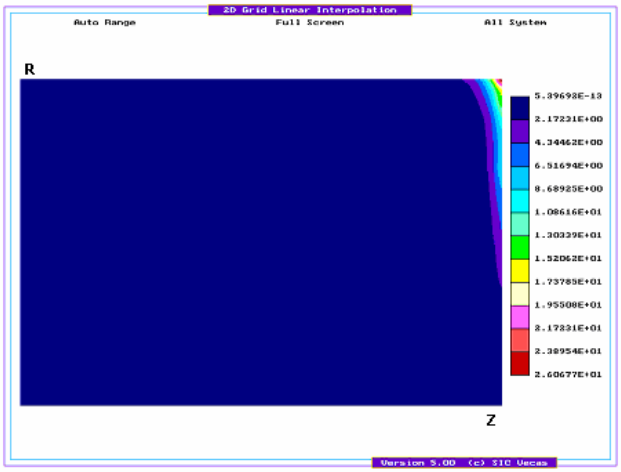

Fig. 2.2.7. Distribution of power in the specimen, W/cm^3

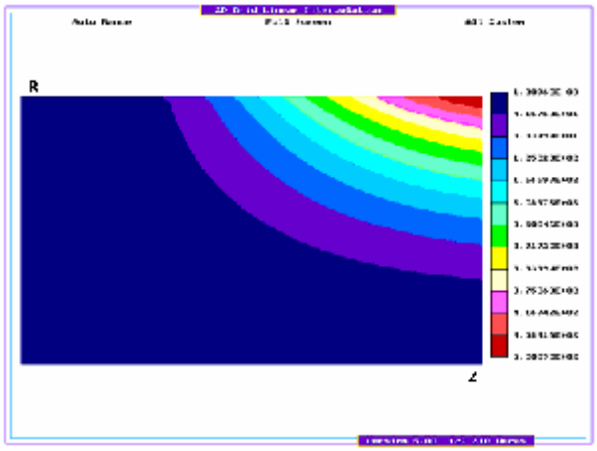

Fig. 2.2.8. Distribution of power in the melt, W/cm^3

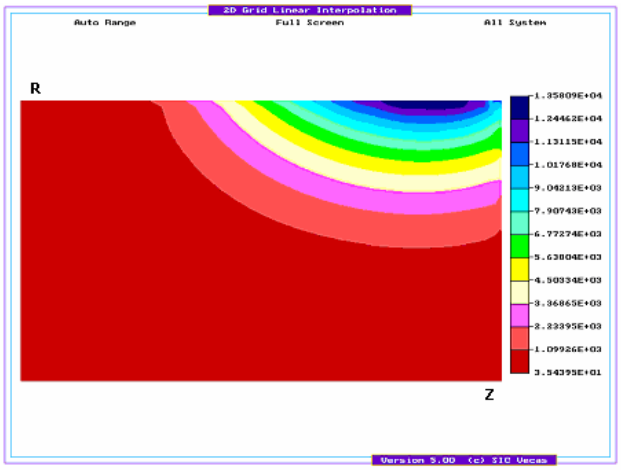

Fig. 2.2.9. Distribution of Lorentz forces in the melt (radial vector component), N/cm^3

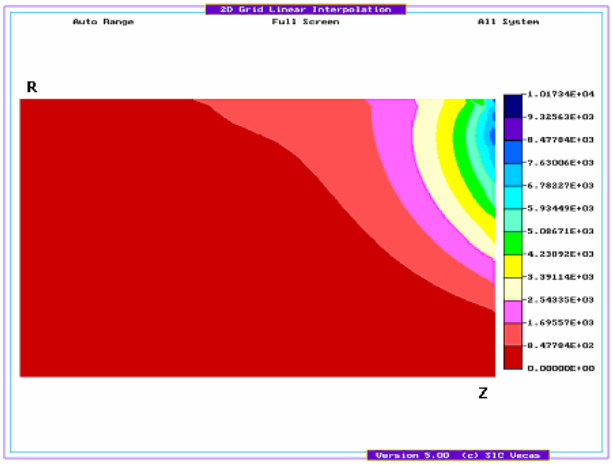

Fig. 2.2.10. Distribution of Lorentz forces in the melt (axial vector component), N/cm^3

The third temperature condition of the specimen (91,052 sec)

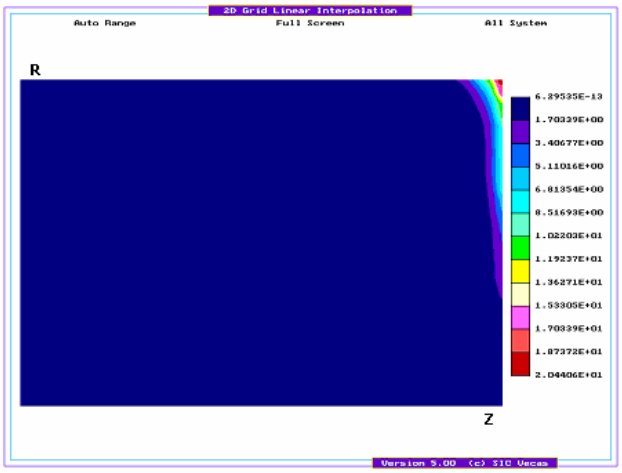

Fig. 2.2.11. Distribution of power in the specimen, W/cm^3

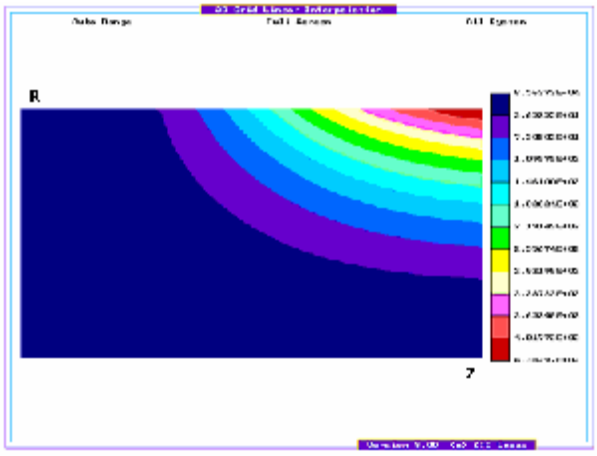

Fig. 2.2.12. Distribution of power in the melt, W/cm^3

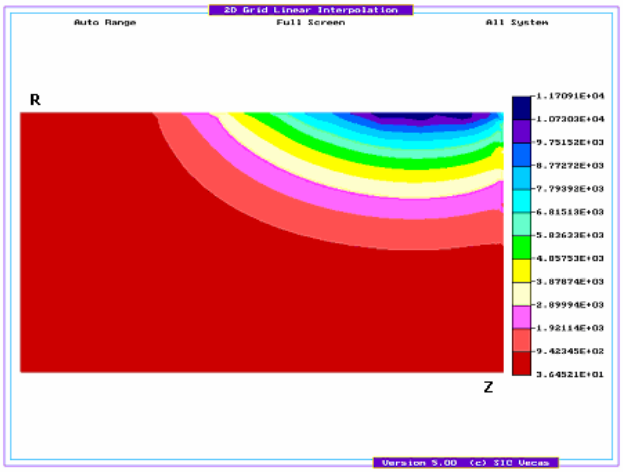

Fig. 2.2.13. Distribution of Lorentz forces in the melt (radial vector component), N/cm^3

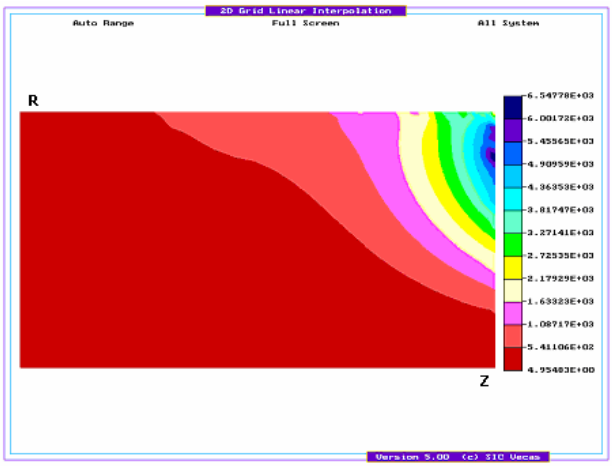

Fig. 2.2.14. Distribution of Lorentz forces in the melt (axial vector component), N/cm^3

The fourth temperature condition of the specimen (132,811 sec)

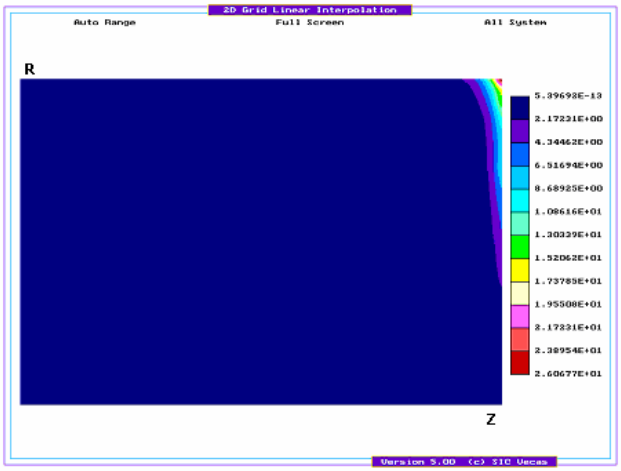

Fig. 2.2.15. Distribution of power in the specimen, W/cm^3

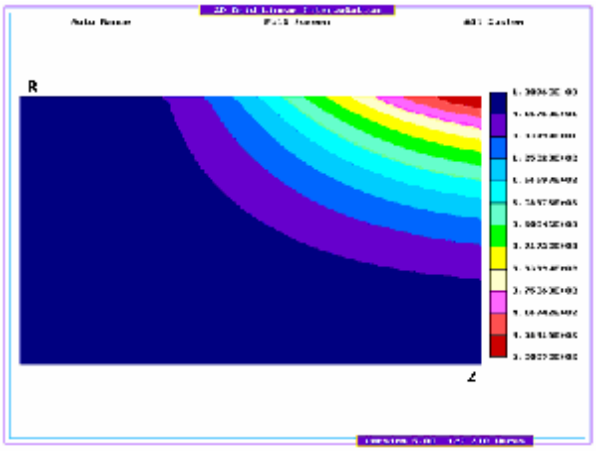

Fig. 2.2.16. Distribution of power in the melt, W/cm^3

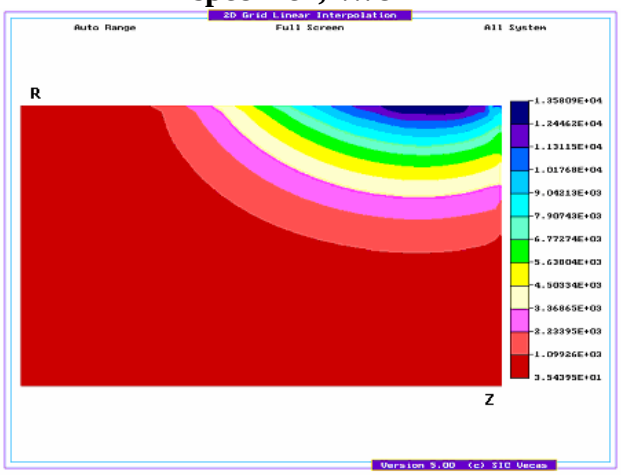

Fig. 2.2.17. Distribution of Lorentz forces in the melt (radial vector component), N/cm^3

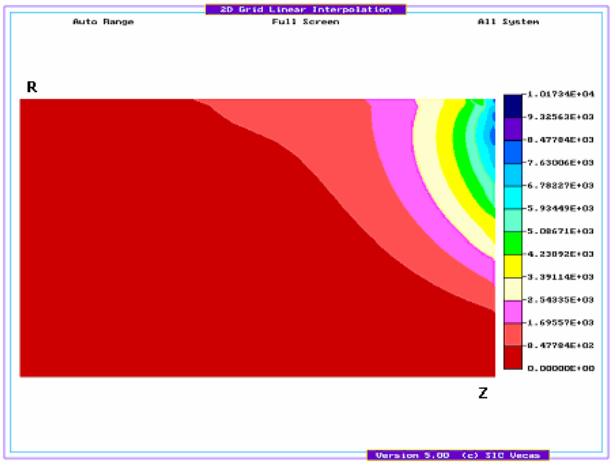

Fig. 2.2.18. Distribution of Lorentz forces in the melt (axial vector component), N/cm^3

2.3. Ultrasonic measurements of the specimen ablation rate

For determining ablation kinetics of the vessel steel specimen, the method of ultrasonic sounding was applied. For its implementation, an artificial acoustic defect was made near the specimen top surface influenced by the temperature. This defect, located beyond the interaction region, was used as a reference point (Fig. 1.1.3.). Its availability significantly increases precision of measurements in comparison with the measurement of the distance between the ultrasonic converter and the observed surface.

The specimen was sounded by a pulse-periodic signal at 100 Hz. During the intervals between the sounding pulses, the ultrasonic converter automatically switched to the echo signal receiving mode. The ultrasonic sensor P 111-2.5-K12 with the natural frequency of 2.5 MHz was used as a converter. A Panametrics oscillator receiver (model 5800) was used as the emitter and echo signal receiver. For the purposes of visualization and setting, the signal was conveyed from the receiver to the Tektronix TDS 210 oscillograph connected to the computer – for analyzing and processing the received information. To this end, a programme was developed in the LabView environment for the continuous mathematical treatment of data. This treatment resulted in values of distances from the defect to specimen surface, taking into account the temperature gradient between the echo signal reflecting surfaces.

The displayed echo signal images represented two groups of oscillations. The left one corresponded to the echo signal from the defect, while the right one – to that from the specimen top. The basic frequency of oscillations in both groups coincided with the natural resonance frequency of the ultrasonic converter, but the spectral composition differed between the groups. Fig. 2.3.1 shows an example of echo signals observed on the monitor in the course of the test.

In-phase half waves were chosen, one per each group. Then, on each half-wave two points were taken – one at the zero line crossing and the other one at an amplitude extreme. Later on, the changes in time delay between the point pairs were followed. These changes, recalculated taking into account the dependence of acoustic speed in material on the temperature, correspond to changes in the specimen length due to its surface ablation.

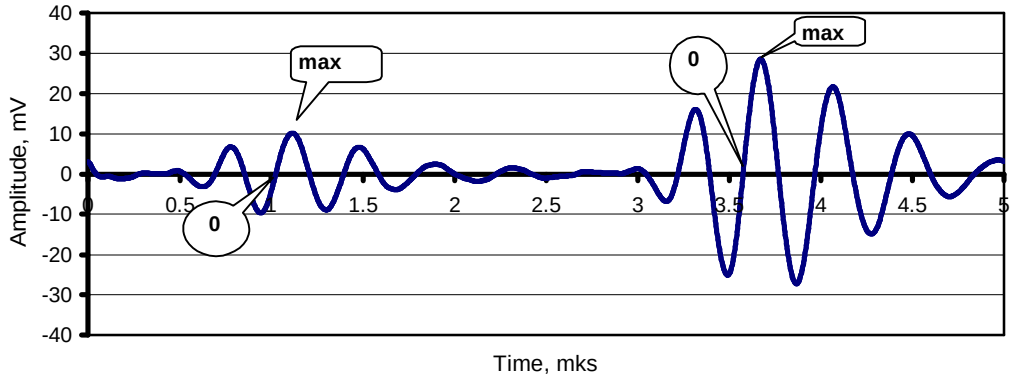

Fig. 2.3.1. Echo signals observed in the test

Fig. 2.3.2 presents the curves showing changes in the distances $D_{zero\ cross}$ (D_{i0}) and D_{peak} (D_{im}), as well as termperature changes at thermocouple locations (Tab. 1.1.1.) near the specimen top throughout the test. The necessity of two types of measurements was conditioned by the echo signal attenuation vs. specimen temperature growth, expressed in its amplitude contraction. A regime might be achieved when the useful signal could merge with the noise and data acquisition by the signal peaks might become problematic. In contrast, the zero line crossing can be determined with sufficient accuracy in the absence of the constant component.

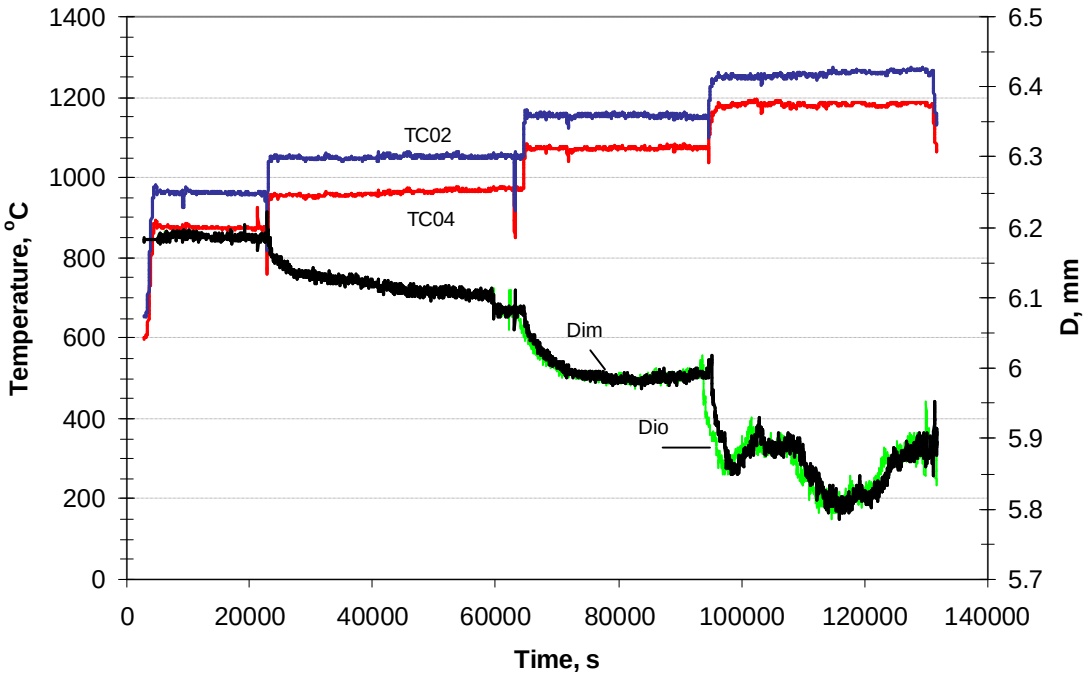

D_{im} – change of the distance between the top and defect (calculated from peak positions); D_{i0} – change of the distance between the top and defect (calculated from zero cross positions).

Fig. 2.3.2. Evolution of temperature at the specimen top and of the distance from the top to defect

The absence of complete overlapping of the $D_{i0}(\tau)$ and $D_{im}(\tau)$ curves in the high temperature domain can be explained by a higher sensitivity of signal amplitudes to temperature changes than that of the values corresponding to zero crossing. On the whole, it may be stated that measurements of both types produce similar results and in future one of them can be chosen depending on peculiarities of the test.

The actual distance D between the reflecting surfaces of the defect and top at 'zero' temperature is expressed as a product of acoustic speed by time:

$$D = \frac{C(0)\Delta t}{2},$$

where $C(0)$ is the acoustic speed in the material in question at 'zero' temperature; Δt is the time between echo signals from the defect and top relative to the chosen reference points.

Taking into account changes of the temperature along the specimen *T(l)*, the measured distance is determined by the formula:

$$D_m = C(0)\int_0^D \frac{dl}{C(T)},$$

where $C(T)$ is the dependence of acoustic speed on temperature.

$$C(T) = \frac{C(0)}{1 + bT(l)},$$

where b is the coefficient allowing for the temperature-dependent changes in the acoustic speed with the constant distance between the defect and top.
It is supposed that

$$T = \frac{T_2 - T_1}{l_2 - l_1} l + \frac{T_1 l_2 - T_2 l_1}{l_2 - l_1},$$

where T_1 is the temperature in the defect region, T_2 is the temperature in the specimen top region, l is the distance from the specimen top to the point of T determination in the gap between the defect and top, l_1 is the distance from the top to the point of T_1 determination, and l_2 is the distance from the top to the point of T_2 determination.
The result of integration is as follows:

$$D_m = D + b \frac{T_1 l_2 - T_2 l_1}{l_2 - l_1} D + \frac{1}{2} b \frac{T_2 - T_1}{l_2 - l_1} D^2 .$$

The coefficient b is calculated on the assumption of equality of the actual D and D_m, distance which is determined from the given formulas when the specimen temperature is changing during its heating or cooling down (without destruction). For the conditions of the test, the numeric value of b was determined to be $2 \cdot 10^{-4}$.

Finally,

$$D = \frac{2 D_m}{\left(1 + b \frac{T_1 l_2 - T_2 l_1}{l_2 - l_1}\right) + \sqrt{\left(1 + b \frac{T_1 l_2 - T_2 l_1}{l_2 - l_1}\right)^2 + 2b \frac{T_2 - T_1}{l_2 - l_1} D_m}} .$$

Data processing and analysis have shown that with the growth of the specimen temperature not only the signal transmission speed was changing, but also its amplitude and the spectral composition. Presumably, it is conditioned by the changes in the specimen material structure under the influence of high temperature. According to the results of the microstructure analysis, the border of structural changes lies between the defect and top, therefore these changes significantly influence the measurements of distance. A comparison of the final distance between the defect and top measured by ultrasonic sounding with that measured by microscopy showed them to coincide sufficiently well.

2.4. Physico-chemical analysis

2.4.1. Material balance

After the natural cooling of the ingot in argon, the furnace was depressurized, the vessel steel specimen and products of melting were extracted from the crucible, sorted and weighed to within 0.1 g. The material balance for the test is given in Tab. 2.4.1.

Table 2.4.1.

Material balance

Introduced, g		Collected, g	
Steel specimen	1723.0	Steel specimen	1724.9
Main charge, C-100	1779.6	Corium ingot	1581.7
Start-up material, Zr	15.1	Crust above the melt	107.3
Correcting addition, UO_2	168.1	Aerosols	114.0
		Samples	87.5
		Spillages	60.7
Total	3685.8	**Total**	3676.1
Debalance, g		-9.7	

The debalance is explained by the loss of a part of aerosols while cleaning of the clogged gas circuit during the test.

2.4.2. Chemical analysis of melt samples and corium ingot

The samples of molten corium taken during the test and the corium ingot were analyzed for the content of U^{+4} and U^{+6}. The analysis was done using average samples taken by quartering and crushed to particles sized below 50 μm.

The technique of U^{+4} and U^{+6} determination with arsenazo III reagent is meant for the determination of uranium microquantities in corium samples without uranium separation, with a sensitivity of 0.04 μg/ml [5]. The technique allows determination of uranium (IV) and the total uranium in the solution. The quantity of uranium (VI) is calculated from the difference between the content of uranium (IV) and total uranium. The results of chemical analysis of molten corium samples and the ingot are given in Tab. 2.4.2.

Table 2.4.2.

Results of corium chemical analysis

Composition	Sample 1	Sample 2	Sample 3	Sample 4	Sample 5	Sample 6	Sample 7	Ingot
	mass %							
U^{+4}	63.7	62.1	63.7	61.9	61.2	62.2	60.1	63.9
In terms of **UO_2**	72.2	70.4	72.3	70.2	69.4	70.6	68.2	72.4

U^{6+} was not found in the samples. The relative error of U^{+4} and U^{+6} content determination was not more than 2 %.

2.4.3. Fused corium density

Determination of fused corium pycnometric density was carried out using an average sample obtained by quartering. Distilled water was used as the pycnometric fluid. The results of density determination under normal conditions are given in Tab. 2.4.3.

Table 2.4.3.

Results of fused corium pycnometric density determination

Fused corium particle size, μm	**Pycnometric density, g/cm^3**
100-200	**8.52**
<50	**8.65**

The error of density determination was ± 0.02 g/cm^3.

The results of posttest physico-chemical analyses lead to a conclusion that practically only uranium oxides were evaporating from the melt during the test. The amount of uranium oxide evaporated from the melt in the test was ~ 114.0 g. The average specific rate of uranium oxide evaporation at the first steady-state regime was ~ 88.5 mg/cm^2·h. It was impossible to evaluate the uranium oxide evaporation rate at other regimes due to clogging of the aerosol collecting line and aerosol accumulation on the shaft and crucible walls.

The debalance between the evaporated and added masses of uranium oxide, as well as the breaking down of crusts into the melt when cleaning the crucible sections at the last steady-state regime were the major reasons of the change in the final melt composition if compared to the initial one.

2.5. SEM/EDX analysis of corium and steel

2.5.1. Oxidic ingot

The analysis of oxidic ingot showed that its top, bottom, central and side parts practically have the composition of the initial corium. (see Tab. 2.5.1, Fig. 2.5.1 – regions SQ1, SQ2, SQ3, SQ4, SQ5 and SQ).

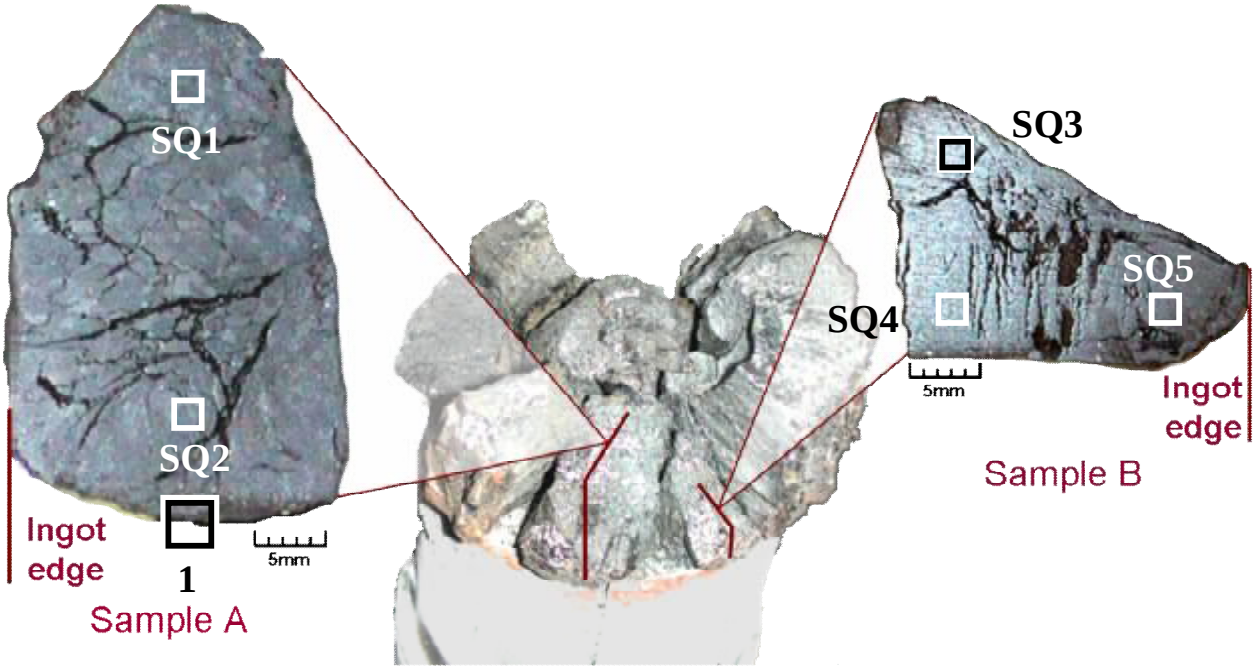

Fig. 2.5.1. Diagram of templates cutting from the corium ingot (samples A and B)

As is evident from Fig. 2.5.2., a layered oxidic structure is observed at the interface between the oxidic and metallic parts. The lowest part of the ingot of about 0.8 mm thick, has a homogeneous structure and a composition close to the average composition of the oxidic ingot. This region is likely to consist of sintered initial C-100 corium layer (crust, Item 1.1). This is confirmed by the porous structure of this region (with a large number of small pores, unlike the rest of the ingot which is either nonporous or has large pores). Next to this region of sintered oxides is a thin layer predominantly consisting of uranium oxides. Above is a mixed oxidic layer, with a UO_2/ZrO_2 molar ratio of ≈1:2. In accordance with the data of [6], this corresponds to the liquidus – solidus point of contact from the most refractory phase side. It should be noted that the

obtained results show that the high-temperature part of the UO_2-ZrO_2 constitution diagram plotted by the above authors corresponds to the test more than the diagram given in [7].

Table 2.5.1.

Results of templates EDX analysis, samples A and B

№		U	Zr	O
SQ1	mass %	64.0	20.3	15.7
	mol. %	18.2	15.1	66.7
		UO_2	**ZrO_2**	
	mass %	72.5	27.5	
	mol.%	54.7	45.3	
		U	**Zr**	**O**
SQ2	mass %	64.4	19.9	15.7
	mol.%	18.4	14.9	66.7
		UO_2	**ZrO_2**	
	mass %	73	27	
	mol.%	55.3	44.7	
		U	**Zr**	**O**
SQ3	mass %	63.7	20.6	15.7
	mol.%	18.1	15.2	66.7
		UO_2	**ZrO_2**	
	mass %	72.3	27.7	
	mol.%	54.4	45.6	
		U	**Zr**	**O**
SQ4	mass %	63.9	20.4	15.7
	mol.%	18.2	15.1	66.7
		UO_2	**ZrO_2**	
	mass %	72.5	27.5	
	mol.%	54.7	45.3	
		U	**Zr**	**O**
SQ5	mass %	64.5	19.8	15.7
	mol.%	18.5	14.8	66.7
		UO_2	**ZrO_2**	
	mass %	73.3	26.7	
	mol.%	55.6	44.4	
SQ- molten corium composition (rapid analysis)		**UO_2**	**ZrO_2**	
	mass %	73	27	
	mol.%	55.3	44.7	

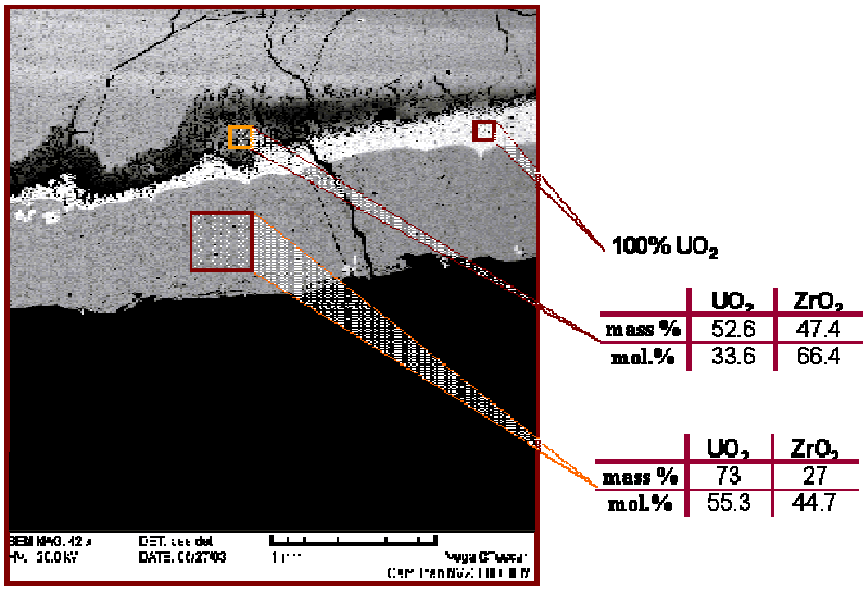

Fig. 2.5.2. SEM image and EDX analysis results of template region 1, sample A (see Fig. 2.5.1)

The presence of the described regions allows a conclusion that about 1 mm above the steel specimen there was a layer of crust separating the steel and molten oxides. It should be noted that neither the crust layer, nor the corium bulk contains iron oxides (see Fig. 2.5.1. and Tab. 2.5.1.). From this we assume that steel corrosion products remain localized in a narrow region between steel and crust layer. Under these conditions, oxidation could be limited either by oxygen transfer through the layer of solid oxides, or by iron transfer through the iron oxides layer, or by chemical processes at the metal-oxide boundary.

2.5.2. Steel specimen

For the analysis, a template was cut from the specimen in the form of a plate. SEM/EDX analysis of the plate has found no differences in its chemical composition along its height and radius (see Fig. 2.5.3). At the same time, a higher porosity was observed closer to the metal-oxide interaction boundary, especially in the central part of the ingot.

	Fe	Cr	Ni	Mn	Mo	Si
масс.%	94.4	2.3	1.2	0.3	1.0	0.8
мол.%	93.9	2.5	1.1	0.3	0.6	1.6

	Fe	Cr	Ni	Mn	Mo	Si
масс.%	95.4	2.2	1.6	0.4	0.2	95.4
мол.%	95.0	2.4	1.5	0.4	0.7	95.0

	Fe	Cr	Ni	Mn	Mo	Si
масс.%	95.1	2.4	1.3	0.3	0.5	0.4
мол.%	94.9	2.6	1.2	0.3	0.3	0.7

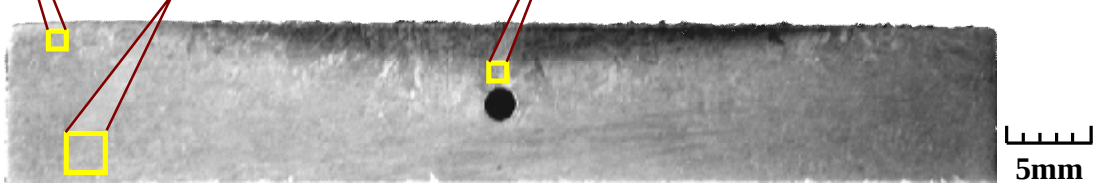

Fig. 2.5.3. SEM/EDX analysis results for various parts of the steel specimen

The formation of pores in this part of the steel ingot may be explained either by a more active recrystallization leading to a larger pore size, or by the carbon burnout in the intergranular space.

2.5.3. The metal-oxide interaction boundary

Fig. 2.5.4. shows the locations of metal-oxide interaction examinations.

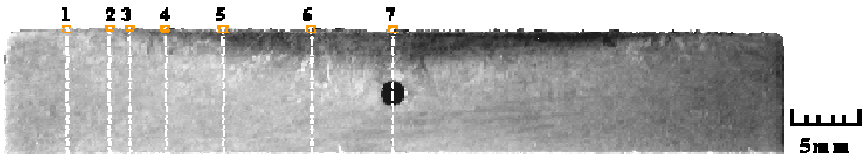

Fig. 2.5.4. Locations of metal-oxide interaction examinations

SEM/EDX analysis of metal-oxide interaction boundary (from periphery to the metallic ingot centre) showed the inhomogeneity of the interface microstructure and phase composition (see Figs. 2.5.5 – 2.5.11).

Closer to the specimen periphery, approximately 1/3 of the distance from the edge to centre, a distinct iron oxide area adjacent to the steel specimen is found. In the peripheral part, the corrosion layer is represented by a FeO-based phase (see Fig. 2.5.5.). Above it, there is an oxidic layer composed of UO_2, ZrO_2 and some aomount of FeO, which confirms the diffusion between the layers of corrosion and sintered crust. It should be noted that the FeO has a rather high porosity.

based phase - FeO

	Fe	Cr	Mn	Si	O
mass.%	75.4	0.5	0.5	0.4	22.6
mol.%	48.1	0.3	0.3	0.5	50.3

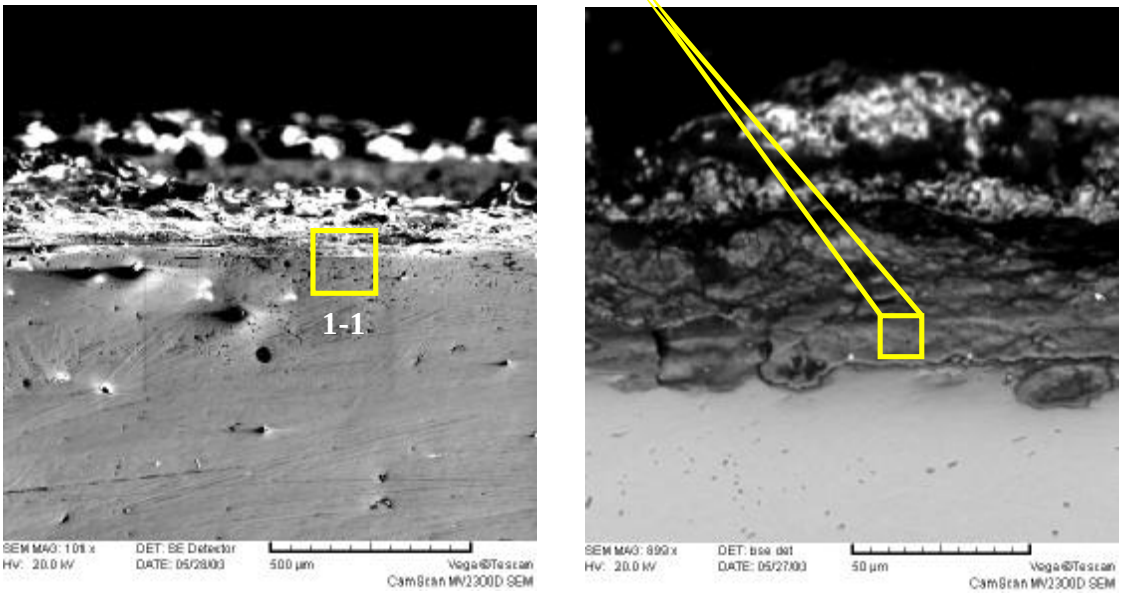

1 **1-1**

Fig. 2.5.5. SEM image and EDX analysis results, region 1 of the metal-oxide interaction boundary (see Fig. 2.5.4)

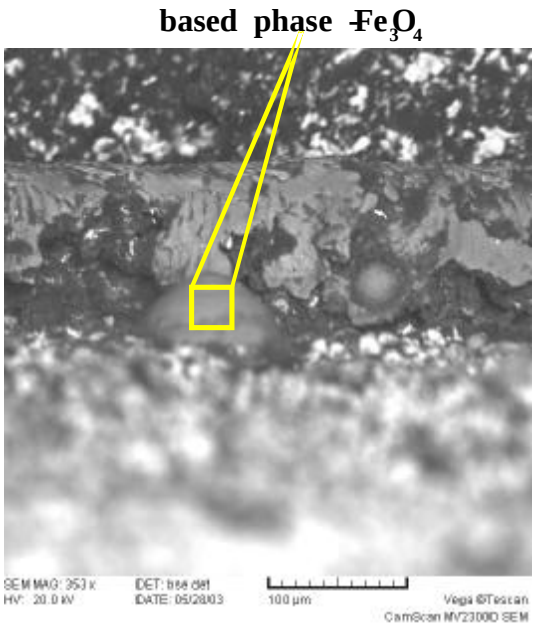

Fig. 2.5.6. SEM image and EDX analysis results, region 2 of the metal-oxide interaction boundary (see Fig. 2.5.4)

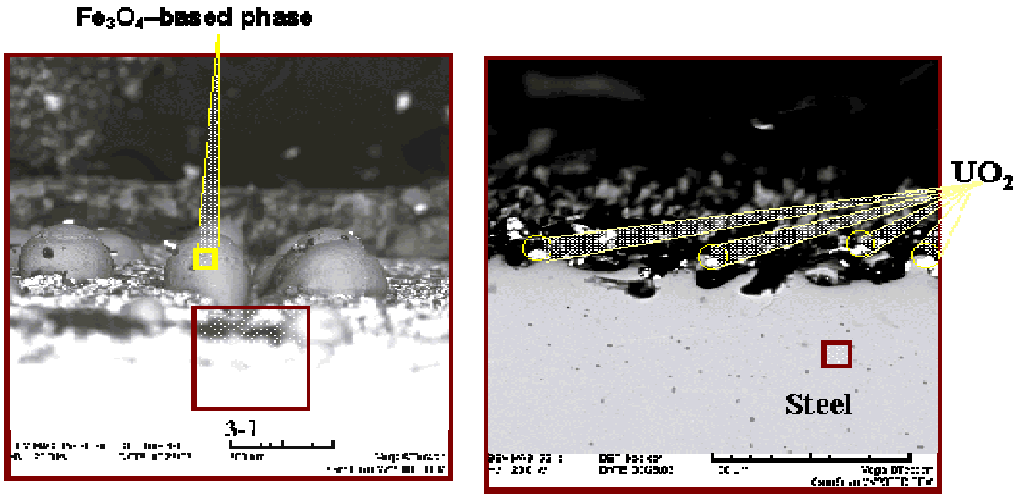

Fig. 2.5.7. SEM image and EDX analysis results, region 3 of the metal-oxide interaction boundary (see Fig. 2.5.4)

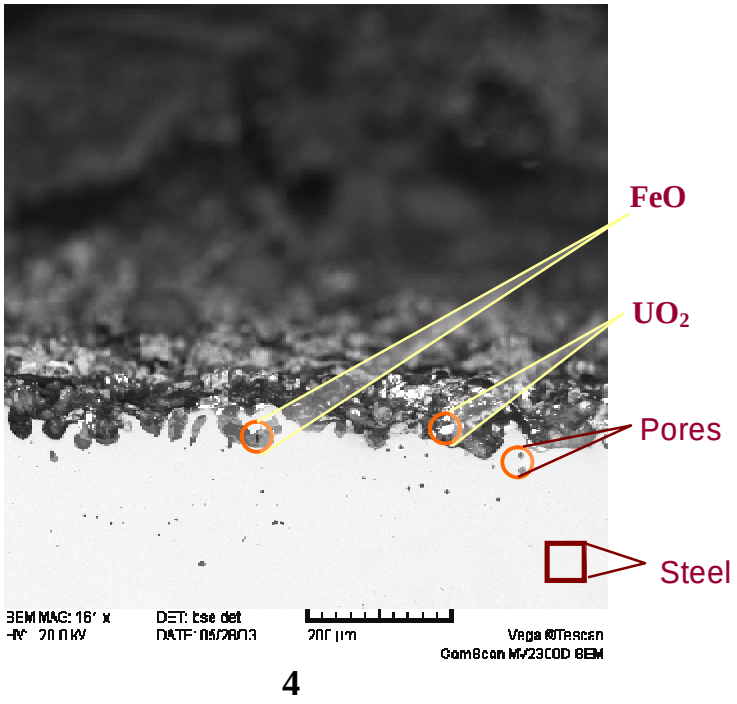

Fig. 2.5.8. SEM image and EDX analysis results, region 4 of the metal-oxide interaction boundary (see Fig. 2.5.4)

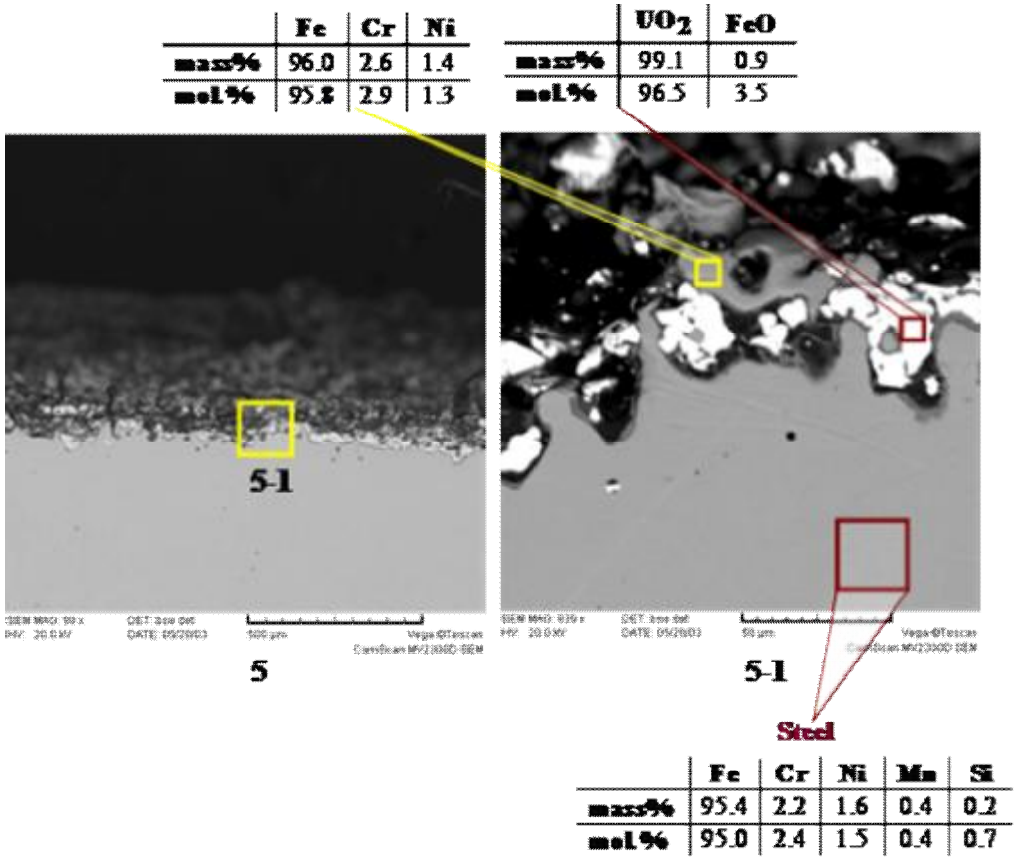

Fig. 2.5.9. SEM image and EDX analysis results, region 5 of the metal-oxide interaction boundary (see Fig. 2.5.4)

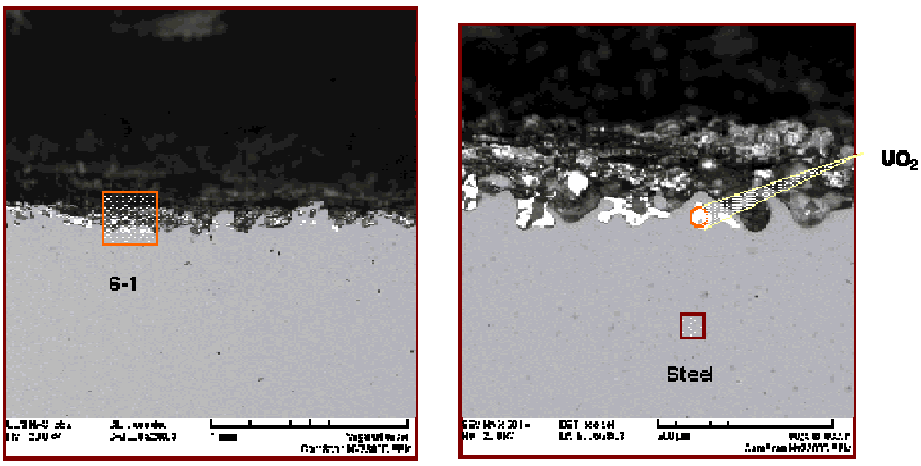

6 6-1

Fig. 2.5.10. SEM image and EDX analysis results, region 6 of the metal-oxide interaction boundary (see Fig. 2.5.4)

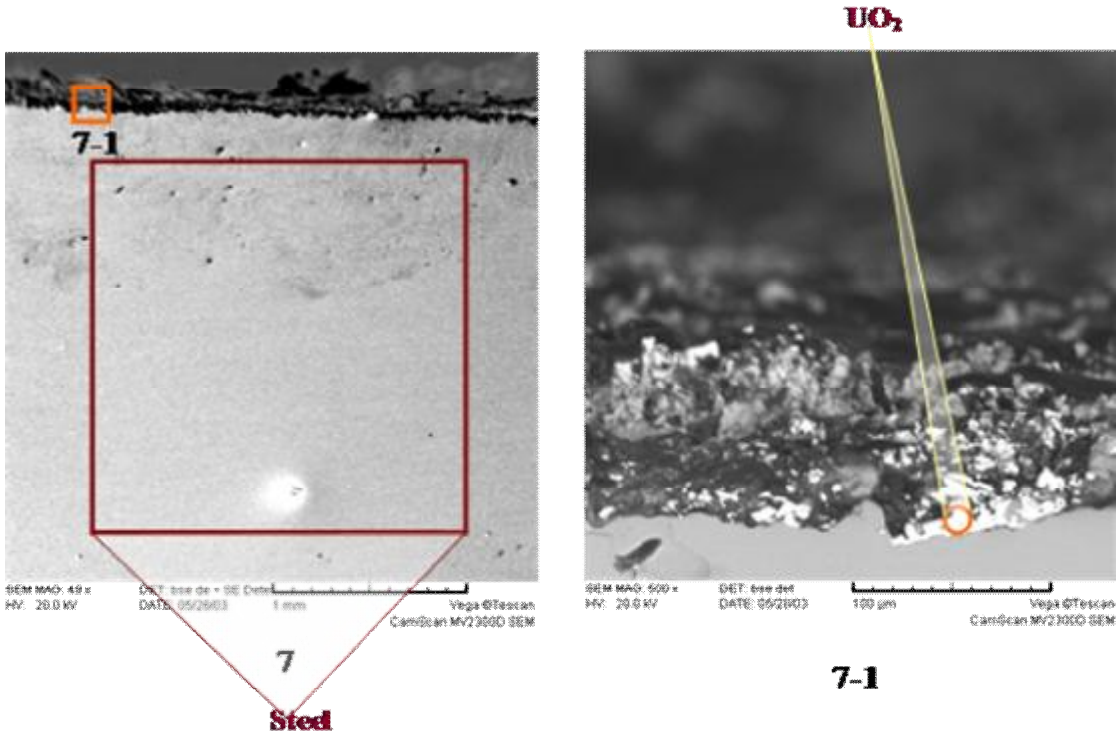

	Fe	Cr	Ni	Si
mass%	95.5	2.4	1.4	0.5
mol%	94.8	2.6	1.3	0.9

Fig. 2.5.11. SEM image and EDX analysis results, region 7 of the metal-oxide interaction boundary (see Fig. 2.5.4)

Closer to the centre – regions 2 and 3, iron oxide separation in the form of Fe_3O_4 (see Figs. 2.5.6, 2.5.7) was observed at the interaction boundary of the oxidic corrosion layer and the layer of uranium and zirconium oxides which had interacted with iron oxide. The presence of a rather significant amount of uranium oxide in this region should be noted. In terms of its microstructure and phase composition, this region is well distinguished from the FeO-based region adjacent to steel, and from the region of sintered corium. In this relation, it may be supposed that said region was formed through crystallization of the molten part of the iron oxide-based corrosion film, which was richer in oxygen than the part of the film that was adjacent to the metallic ingot and

contained some amount of uranium oxide (see Figs. 2.5.6, 2.5.7) that had transited into the melt from the sintered corium layer.

On the approach to region 3 (see Fig. 2.5.7), a higher content of spheroid Fe_3O_4 isolates was observed in the corrosion film, which confirms an increased oxygen content in the part of the film that was in molten state. At the same time, it should be noted that starting from region 4 (see Fig. 2.5.8) an increased thickness of the molten part of oxides (practically to the metallic ingot) was observed, it being confirmed by isolation of uranium oxide at the metal-oxide interaction boundary (light-colour inclusions in Fig. 2.5.8). The relief of metallic surface allows a supposition that starting from region 3 the metal was also in molten state at the metal-oxide interaction boundary. A similar picture was also observed in other regions approaching the centre of the ingot, i.e. in regions 5 (see Fig. 2.5.9) 6 (see Fig. 2.5.10), 7 (see Fig. 2.5.11), respectively. Molten state of metal at the boundary is confirmed by the presence of uranium oxide inclusions in the metal of the boundary area (see Fig. 2.5.10).

On the basis of the obtained results the following conclusions can be made:
1. Depending on the temperature distribution across the specimen top, there may be different regimes of the vessel steel specimen oxidation:

- solid-phase regime– at the specimen edge;
- mixed solid- and liquid-phase regime – in the narrow transitional part between the peripheral and central parts of the specimen;
- liquid-phase regime – in the middle part of the specimen.

2. Since the tickness of the corroded layer of metal practically does not depend on the distance from the area of corrosion to the specimen centre, i.e. the temperature and regime of corrosion are irrelevant, it may be supposed that the process of corrosion is limited by the rate of oxygen supply to the corrosion layer, i.e. it may depend on the thickness and temperature of the crust.

3. Steel oxidation in the considered situation may be limited by oxygen transport through the sintered crust layer, or proceed at the expense of the increased uranium oxide non-stoichiometry with oxygen release at the temperature growth. In the first case, a constant rate of corrosion may be expected, while in the second one – a decreasing rate of corrosion film growth in the course of time.

2.6. Specimen metallography

The performed investigations included:

- pre-test inspection of the initial steel;
- analyses of the steel influenced by molten C-100 corium.

2.6.1. Pre-test inspection of steel and corium components

The specimens for the tests were made from 15Kh2NMFA-A vessel steel produced by Izhorskiye Zavody Association for a VVER-1000.

The alloy is a low-alloy high-temperature steel of the pearlitic grade (according to Guillet). When cooled in undisturbed air, the austenite in heated steel undergoes pearlitic transformations and forms a structure of mixed ferrite and pearlite, sorbite, or troostite. The alloy is based on ferrite, the α-solid solution, while the excessive phase is represented by carbides of Fe_3C type of different origin and shape. The low-alloy high-temperature steels containing such alloying elements as chromium, nickel, molybdenum, manganese in quantities varying from percent fractions to 1-2%, possess a set of such special properties as good weldability and hardenability, low tendency to the austenite grains growth and low critical hardening rate. Their main property is a low creep rate under stresses and temperatures within the working range. For example, the total deformation amounts to 1% for 10,000-100,000 hours. As these steels do not contain large

amounts of chromium, they do not possess high heat resistance and they cannot be applied at temperatures over 550 – 580°C. A typical regime of their thermal treatment is the hardening in oil or in air (normalization) with the following tempering at 720 – 750°C. The temperature A_{C1} = 760°C. The structure after hardening is martensite + bainite, while that after tempering is pearlitic.

For the present investigation, blanks (Fig. 2.6.2) have been flame cut from a reactor vessel fragment (Fig. 2.6.1) and used for producing the specimens. The specimens Nos. I – IV were meant for material studies, and the blank No. V was used for producing the specimen to be used in the test.

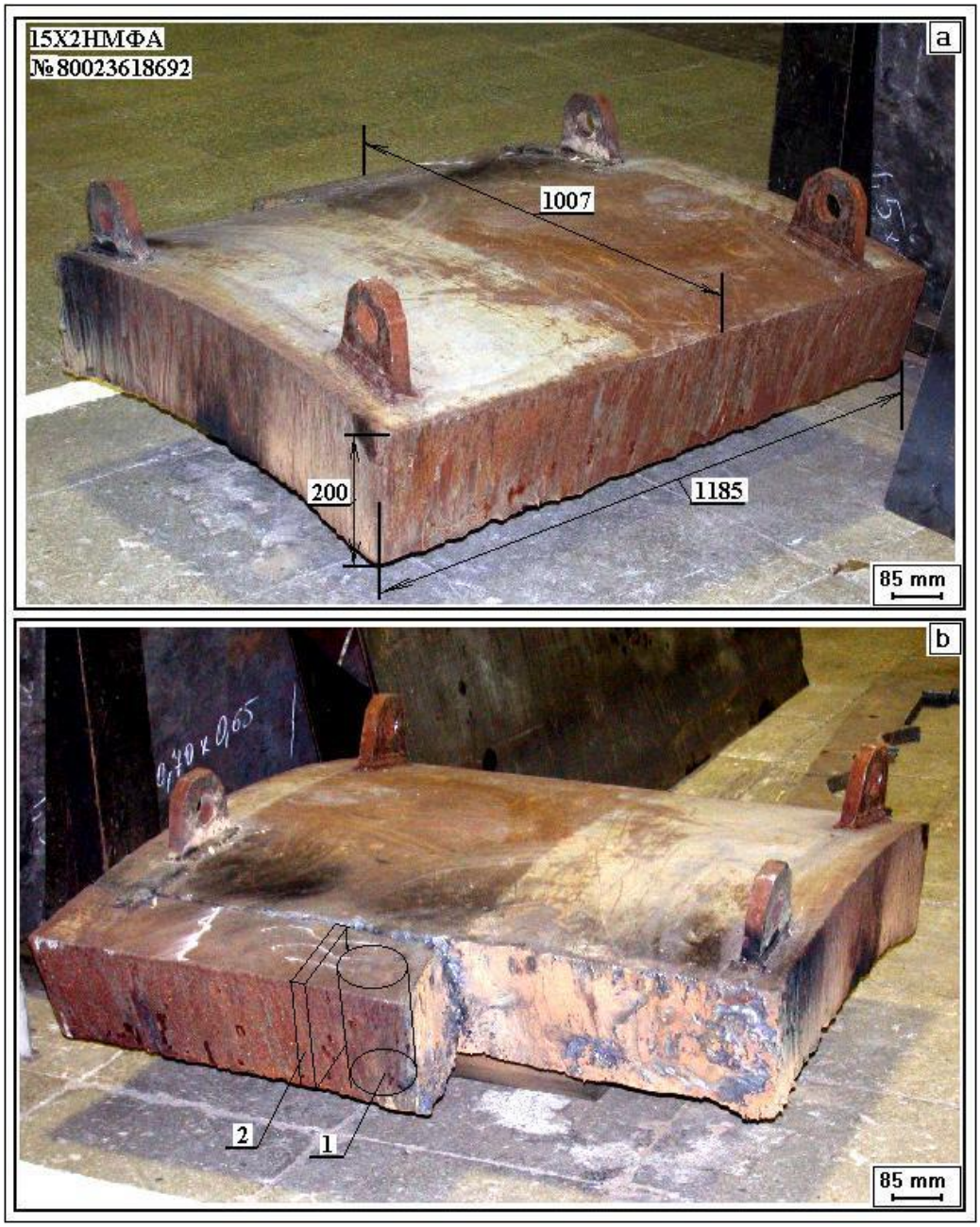

Fig. 2.6.1. Fragment of a VVER-1000 vessel

a – fragment geometry; b – scheme of cutting a specimen for the test (1) and a specimen for the pre-test material studies of steel (2)

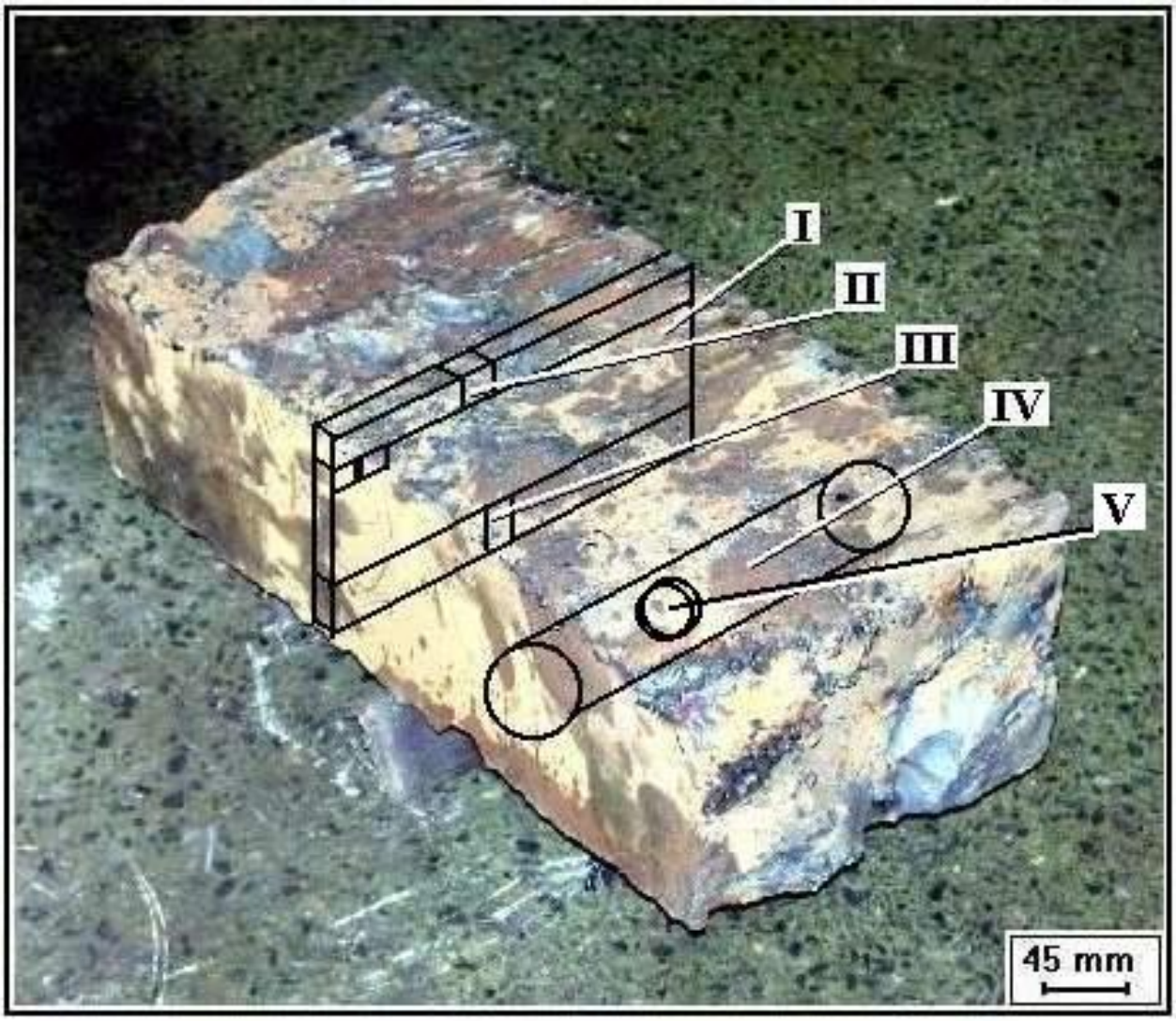

Fig. 2.6.2. Scheme of specimens cutting from blanks
Nos. I - IV – blanks for material studies;
No. V – blank for the tested and reference specimens

Taking into consideration the possible heterogeneity of steel in the specimens, each blank underwent pre-test inspection which consisted of the elemental analysis by XRF and microhardness measurement.

For the elemental analysis, a square specimen No.4 (Fig. 2.6.3) was produced from the blank No.I and a reference specimen (∅ 40 mm) was produced from the blank No.V (Figs. 2.6.4, 2.6.5). The analysis was done using the larger (∅ 40 mm) end surface of the reference specimen.

Fig. 2.6.3. Specimen No. 4 cut from the blank No.I for the control study

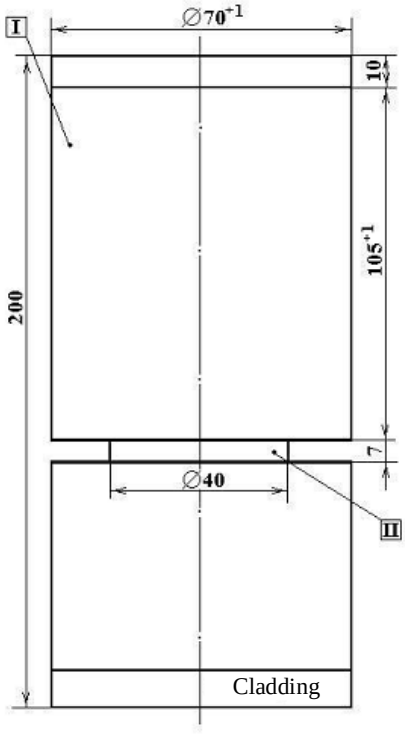

Fig. 2.6.4. Blank No.V cutting plan for producing the tested specimen (I) and the reference specimen (II)

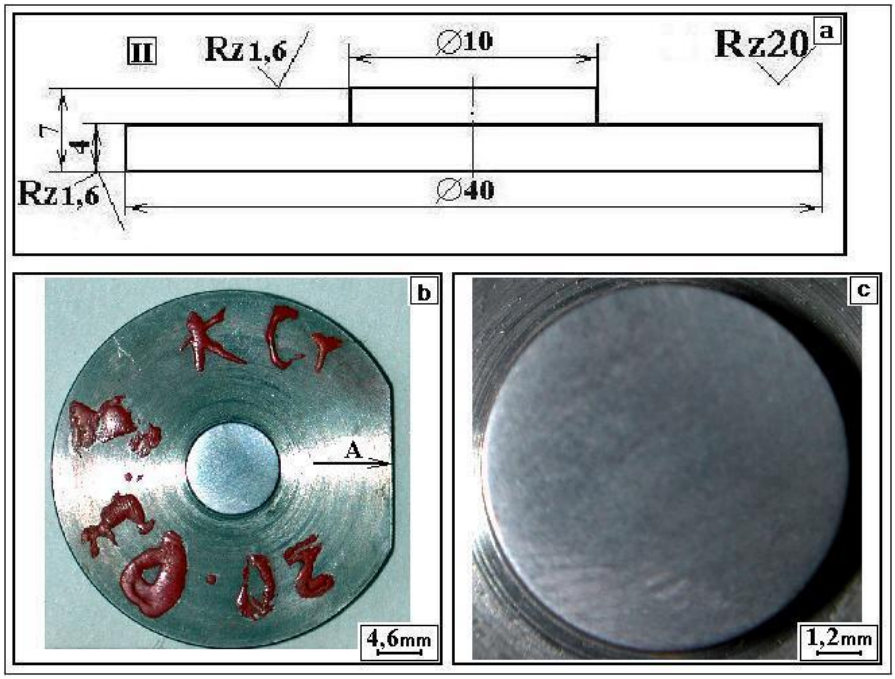

Fig. 2.6.5. Sketch (a) and appearance (b, c) of the reference specimen for the pre-test material study of steel in the blanks

The main steel components content determined by the XRF analysis has proved conformity of the steel with Specs. 108-765-78 for the vessel steel 15KhNMFA-A. Table 2.6.1 offers both the content of the main steel components as given in Specs. of the manufacturer and that determined by the XRF analysis.

Table 2.6.1.

The content of main components in steel

Elements	Element content, %	
	Specs. 108-765-78	XRF
C	0.130 – 0.180	---
Si	0.170 – 0.370	0.250
Mn	0.300 – 0.600	0.490
Cr	1.800 – 2.300	2.240
Ni	1.000 – 1.500	1.002
Mo	0.500 – 0.700	0.704
V	0.100 – 0.120	0.100
P	< 0.020	< 0.020
S	< 0.020	---
Cu	< 0.030	0.068
Co	< 0.030	< 0.030
As	< 0.003	< 0.003

The initial microstructure of the specimen was assessed along the longitudinal section “A” (Fig. 2.6.5, b). The grinding and polishing of the specimen was done according to the standard technique [8]. To reveal the structure, the microsection was treated with etchants for the austenitic, ferritic and pearlitic steels. The microsection surface was photographed at x25 magnification by a NIKON digital camera and by the METALLUX metallographic microscope at x100, x400 and x800 magnifications. The structure (Fig. 2.6.6, a, b, c, d) consists of the finely dispersed ferrite and pearlite. No structural differences have been found between the longitudinal and cross-sections.

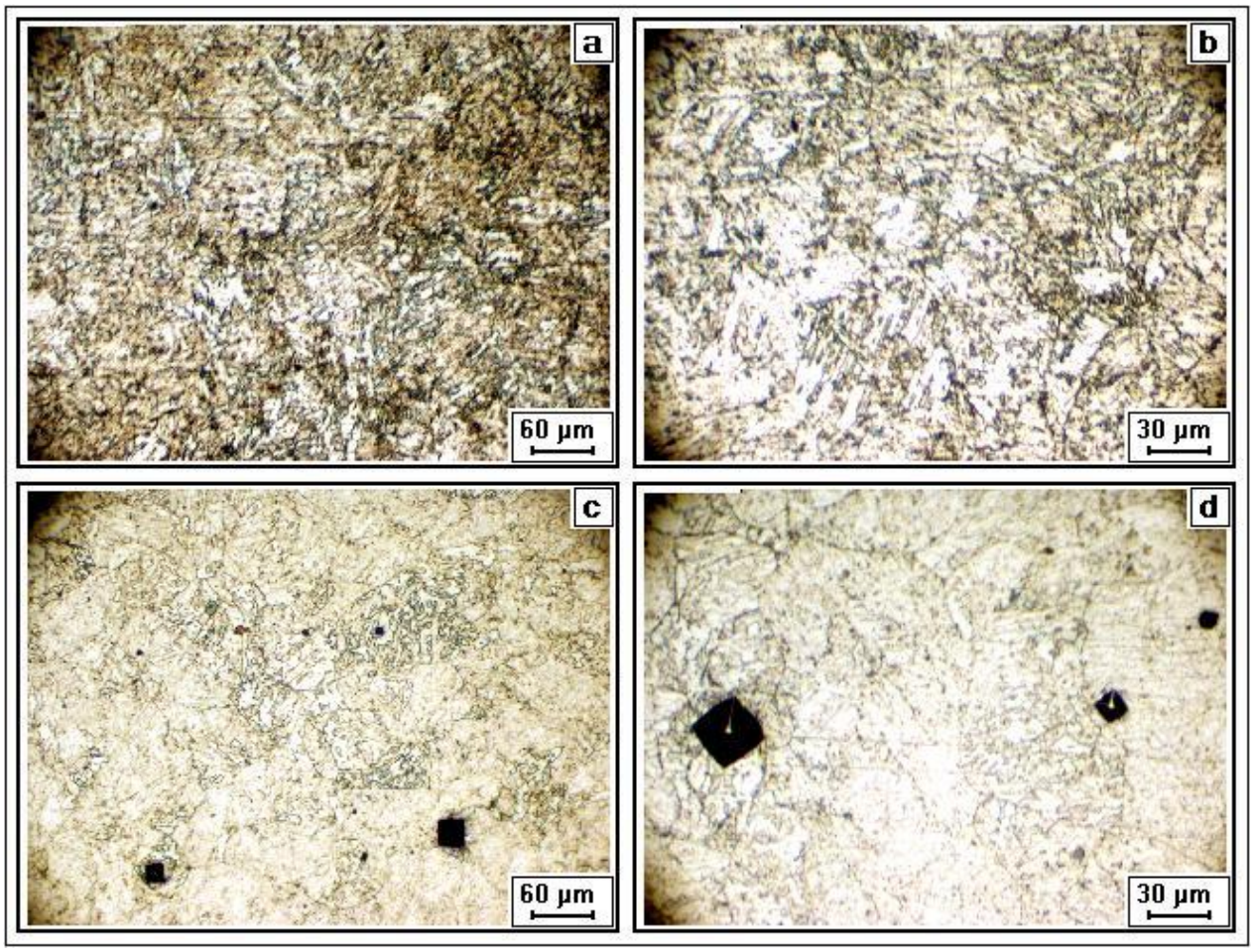

Fig. 2.6.6. Initial steel microstructure in the cross- (a, d) and longitudinal (b, c) sections, with imprints of the diamond pyramid (c, d)

The smaller (∅ 10 mm) end surface of the reference specimen (Fig. 2.6.5) was meant for microhardness measurements. The study employed the PMT-3 microhardness tester and was performed in compliance with requirements of the State Standard 9450 and the 'Procedural guidelines for the PMT-3 microhardness tester' (MI-244). At the loads of 20, 50, 100 and 200 g on the indentor, the diagonal of the diamond pyramid imprints was measured by the MOV-1-15^{x} ocular screw miccrometer at x487 magnification. The accuracy of measurements was ± 0,65 μm. The value of microhardness was determined from 5 imprints. The integral microhardness value for the reference specimen was H_{μ} = 250 – 260.

2.6.2. Measurement of the specimen ablation depth

Under the experimental conditions, a partial ablation of the specimen top occurred at the interaction of corium with the vessel steel specimen. The linear dimension of the specimen along its axis has diminished. However, the ablation was uneven across the top surface, as there were both regular changes along the radius and local pit-shaped ablations (Fig. 2.6.7). To provide a quantitative description of the phenomena, the ablation depth measurements were made and microprofiles of the top section plotted.

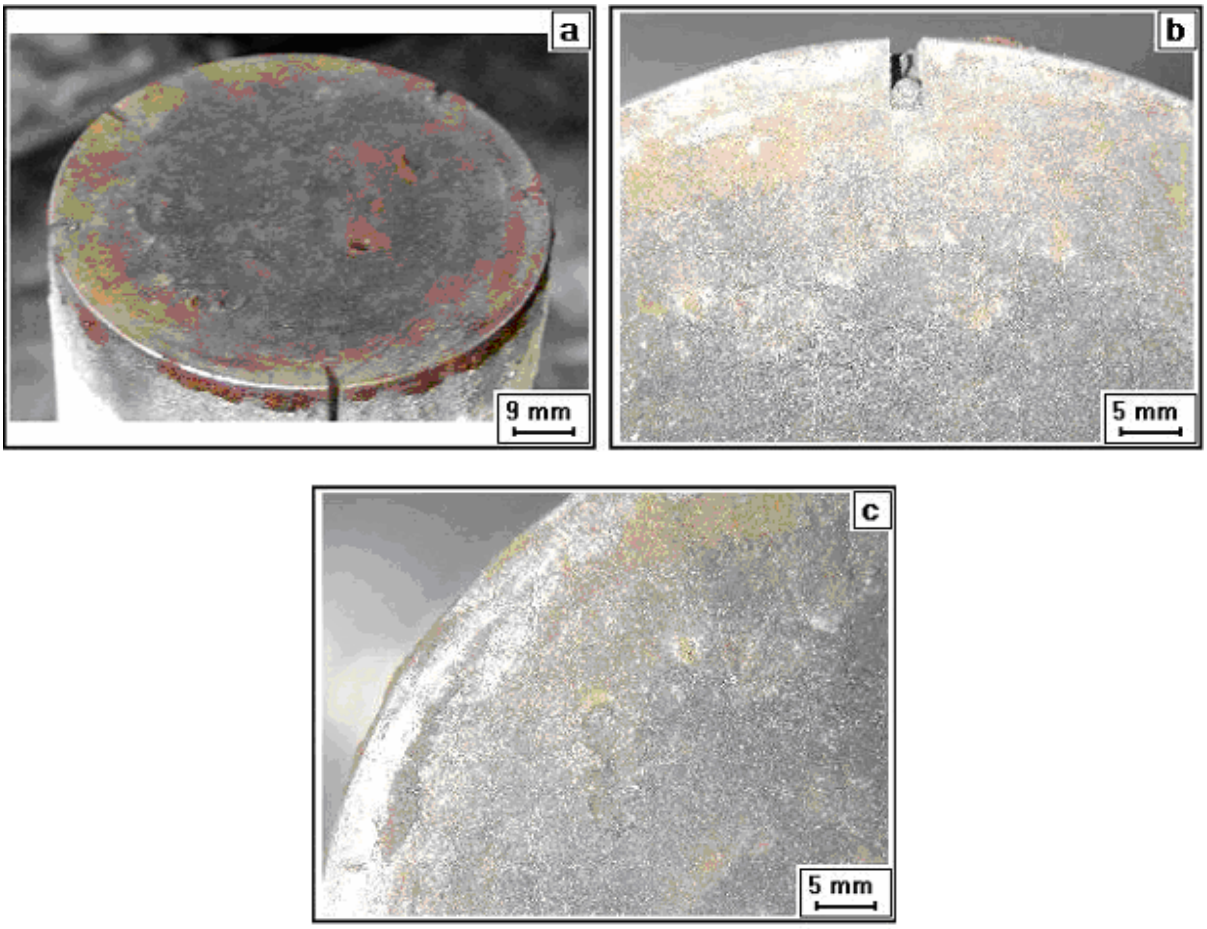

Fig. 2.6.7. Photo of the specimen top and fragments of its surface after the test

Before the test, the initial specimen was measured with the calipers with a scaling factor of 0.02 mm. To provide some datum plane in the cylinder to serve as a reference point for the further measurements, a 1 x 1 mm groove was milled on the specimen side surface at a distance A = 20 mm from the top. The basic distance A was checked on the four cylinder elements diametrical to each other, i.e., $A_1 - A_2$ and $A_3 - A_4$, (Fig. 2.6.8). In order to control precision of the steel specimen manufacturing, the in and out diameters D of the acoustic defect channel drilled horizontally under the top, as well as the distance from it to the top and to the groove were measured (Fig. 2.6.9). The results of measurements are summarized in Tab. 2.6.2.

Table 2.6.2

A_1	A_2	A_3	A_4	B_1	B_2	C_1	C_2	D_1	D_2
19.85	19.76	19.82	19.84	5.20	5.05	14.64	14.70	2.15	2.20

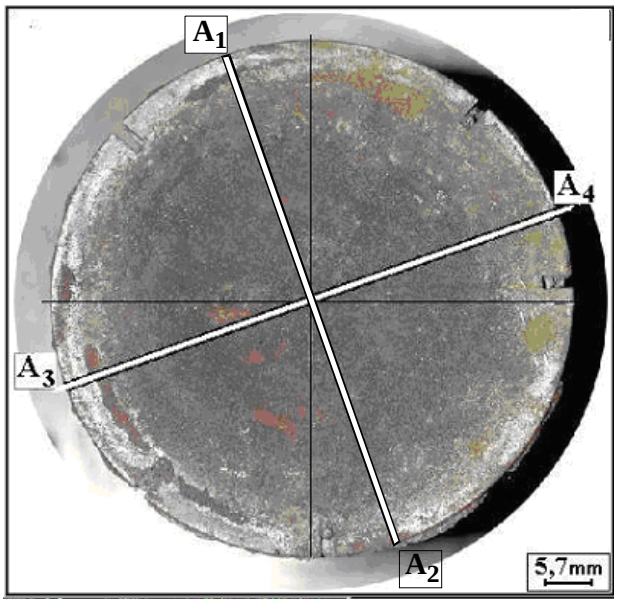

Fig. 2.6.8. Checking diameters of the specimen

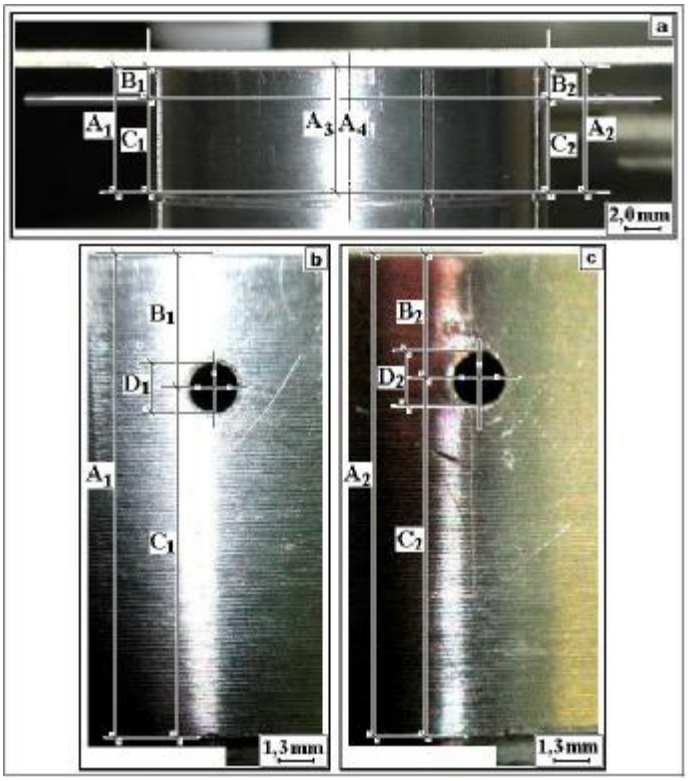

Fig. 2.6.9. Checking distances from the specimen top to the groove

After the test, the specimen was embedded in epoxy and a 30-mm high disk was cut off from the top. Then the disk was cut along the A_3-A_4 diameter, perpendicular to the horizontally drilled channel (Fig. 2.6.10).

Fig. 2.6.10. Template of the specimen upper part longitudinal section along its axis
1 – specimen top; 2 – conventional datum plane

The depth of ablation was measured on a macrosection using the microscope of the PMT-3 microhardness tester at x180 and x487 magnifications, and the BMC-9 stereoscopic microscope at x50 magnification. The combination of two microscopes made it possible to mark the top plane on the microsection (line in Figs. 2.6.12 – 2.6.14) and draw auxiliary hairlines for determining the microrelief size at large magnifications. The depth of ablation was taken as a difference between the initially measured **A** (20 mm, from the top to datum plane) and the height **H** of the corroded surface above the same datum plane. Accuracy of measurements was ± 14 μm. The images of the fragments A, B and C (Fig. 2.6.11) were obtained by respective combining of 25, 20 and 10 photographs (up to x400 magnification), from which profilograms of the surfaces A, B and C were plotted later (Fig. 2.6.12, 2.6.13 and 2.6.14).

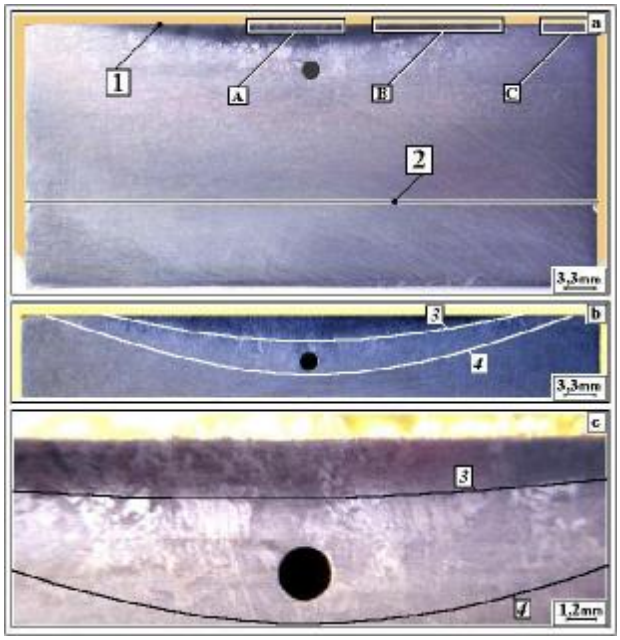

Fig. 2.6.11. Macrostructure of the specimen top, longitudinal section

1 - top; 2- conventional datum plane; 3, 4 – boundaries of the regions of temperature influence on steel structure; A, B, C,- areas of surface microrelief study

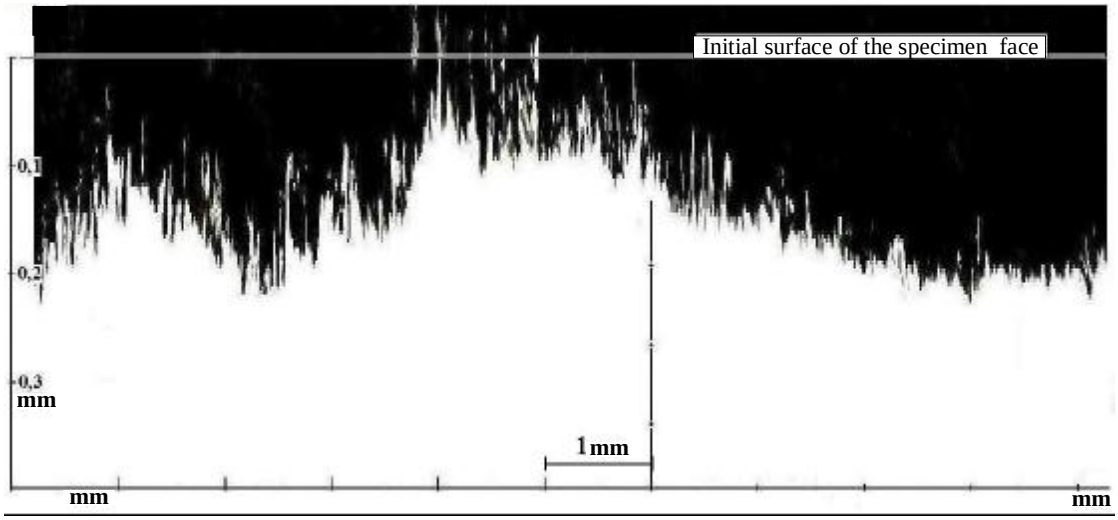

Fig. 2.6.12. Microprofilogram of region A

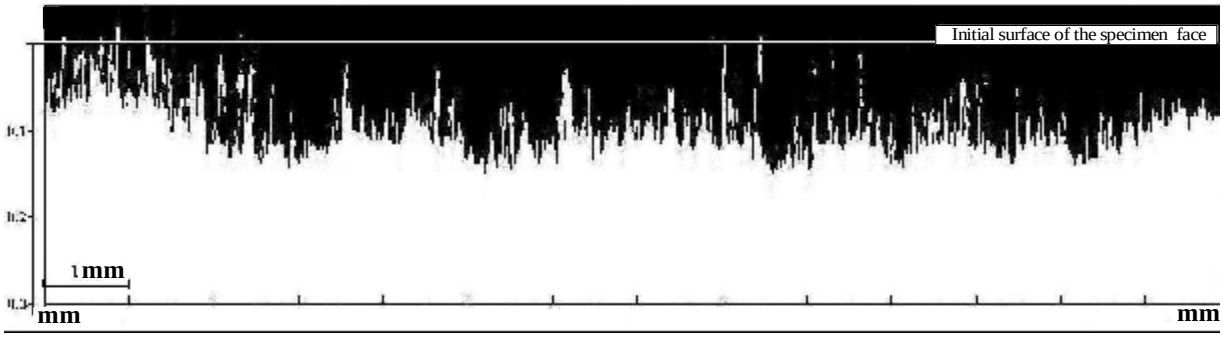

Fig. 2.6.13. Microprofilogram of region B

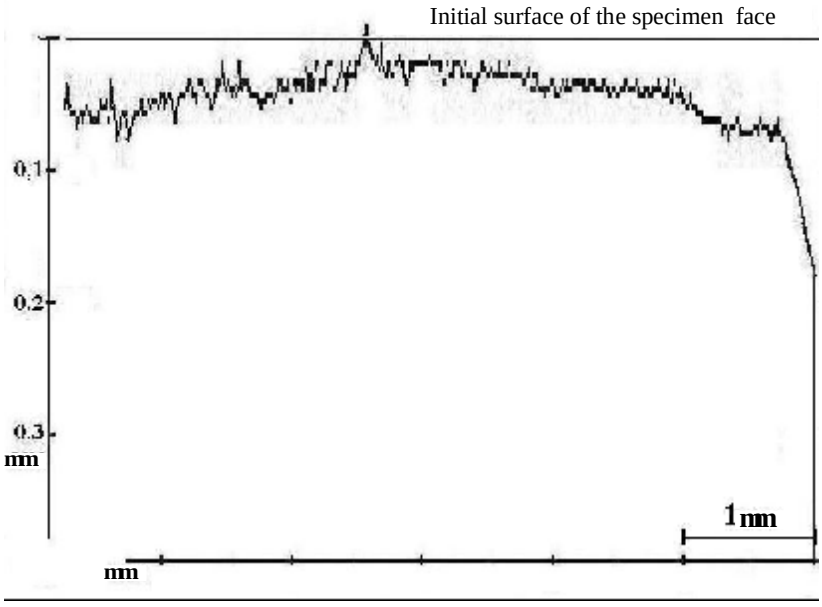

Fig. 2.6.14. Microprofilogram of region C

In each profilogram, the X-line shows the width of the corresponding fragment along the radius of the specimen. The Y-line shows (top-down) the distance from the initial specimen top surface to the actual surface of metal after the interaction.

According to the measurements made in different parts of the specimen section, the depth of ablation amounted to:

- between 20 to 200 μm in the central part of the specimen;
- between 20 to 50 μm on the specimen periphery.

The local pits were beyond the studied section and thus it was impossible to make a conclusion about the depth of corrosion in them.

2.6.3. Steel microstructure after the test

Significant disruption of the surface integrity at the metal-oxide interaction boundary and mixing of metallic and oxidic layers to a depth of 120 – 150 μm was observed (Fig. 2.6.15). The mechanism of mixing reminds that of diffusion welding of dissimilar materials at temperatures close to the temperature of melting of one or both materials. SEM analysis of this region confirmed the supposed molten state of metal, as inclusions of uranium oxide were found inside metal.

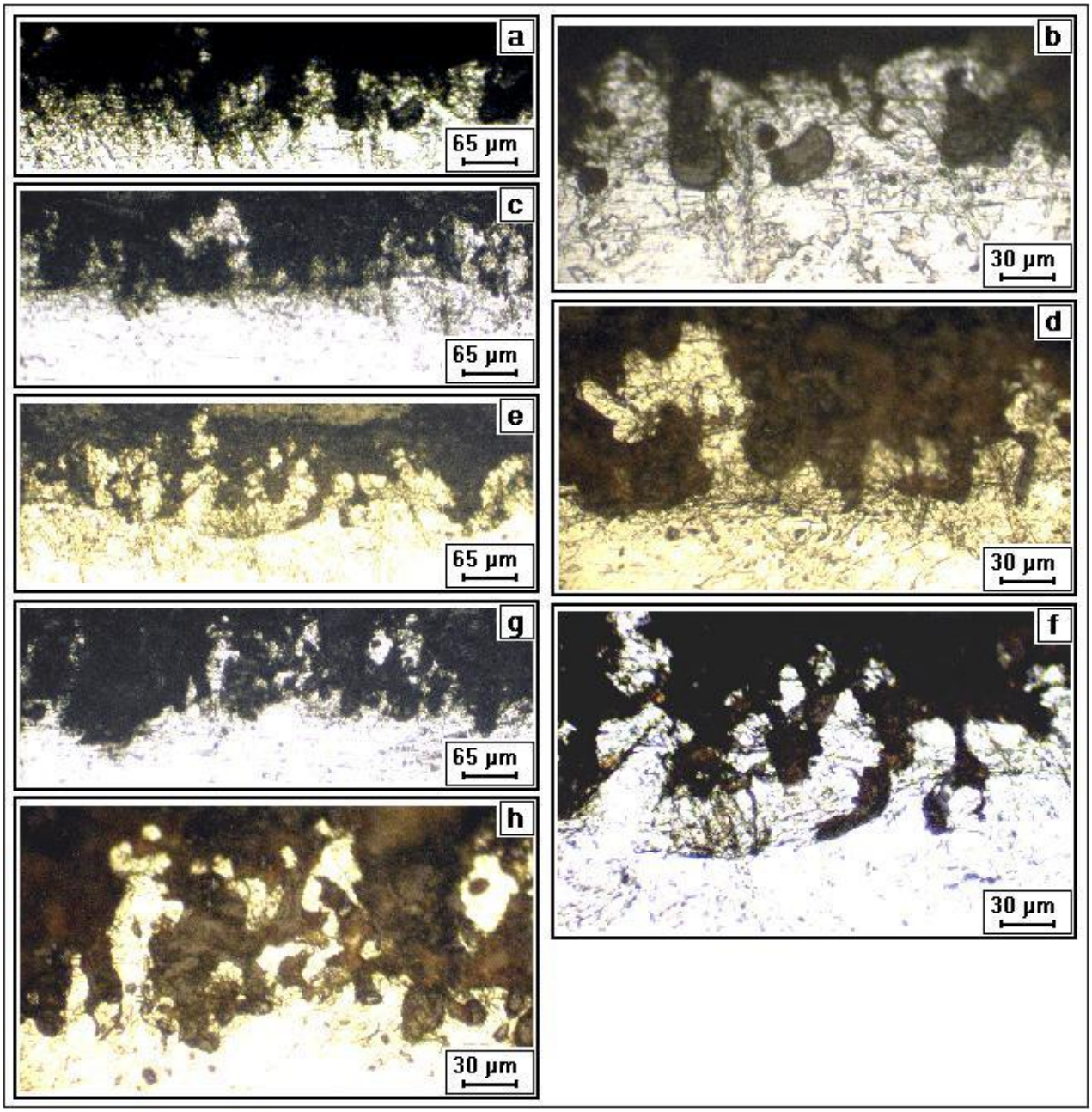

Fig. 2.6.15. Fragments of microprofile in region B

In order to reveal microstructure in the region of thermal influence, the etchants were chosen to both reveal the microstructure, visually determine the area of austenitic transformation along the specimen height, and identify the microstructure.

The macrostructure visible at magnifications not exceeding x50 was delineated by the line 3 (Fig. 2.6.11, b). It is characterized by large grain size and a considerably changed structure of

metal as a result of the austenite complete formation and its transformations during cooling down.

The macrostructure visible at magnifications over x50 was delineated by the line 4. The area between the lines 3 and 4 is characterized by a ferrito-pearlitic structure of austenite decay, as well as by the presence of grains with the initial structure resulting from the austenite incomplete formation during heating. At extreme points, the lines 3 and 4 stretch to a depth of 2.8 - 3.0 mm and 6.8 - 7.0 mm from the top.
The microstructure in the region of complete austenite formation (above line 3) was studied at the locations a, b, i, j and e shown in Fig. 2.6.11, b, c. The microstructure in the region of incomplete austenite formation (above line 4) was studied at the locations c, m, o, g, h and f, also shown in Fig. 2.6.11, b, c. The microstructures of these regions are given in Figs. 2.6.17 - 2.6.19.

The observed structure was of ferrito-pearlitic type that originated at continuous cooling of austenite that had been superheated up to 1000 - 1300°C, i.e., with a very coarse grain. The condition of metal at heating the specimen top, namely the coarse-grain austenite that formed as a result of long-term (several hours) heating up to 1100 - 1300°C, is an important finding of the present work, as the grain size and the area of intergranular boundaries are likely influence the diffusivity and oxygen transport in the region of chemical interaction.

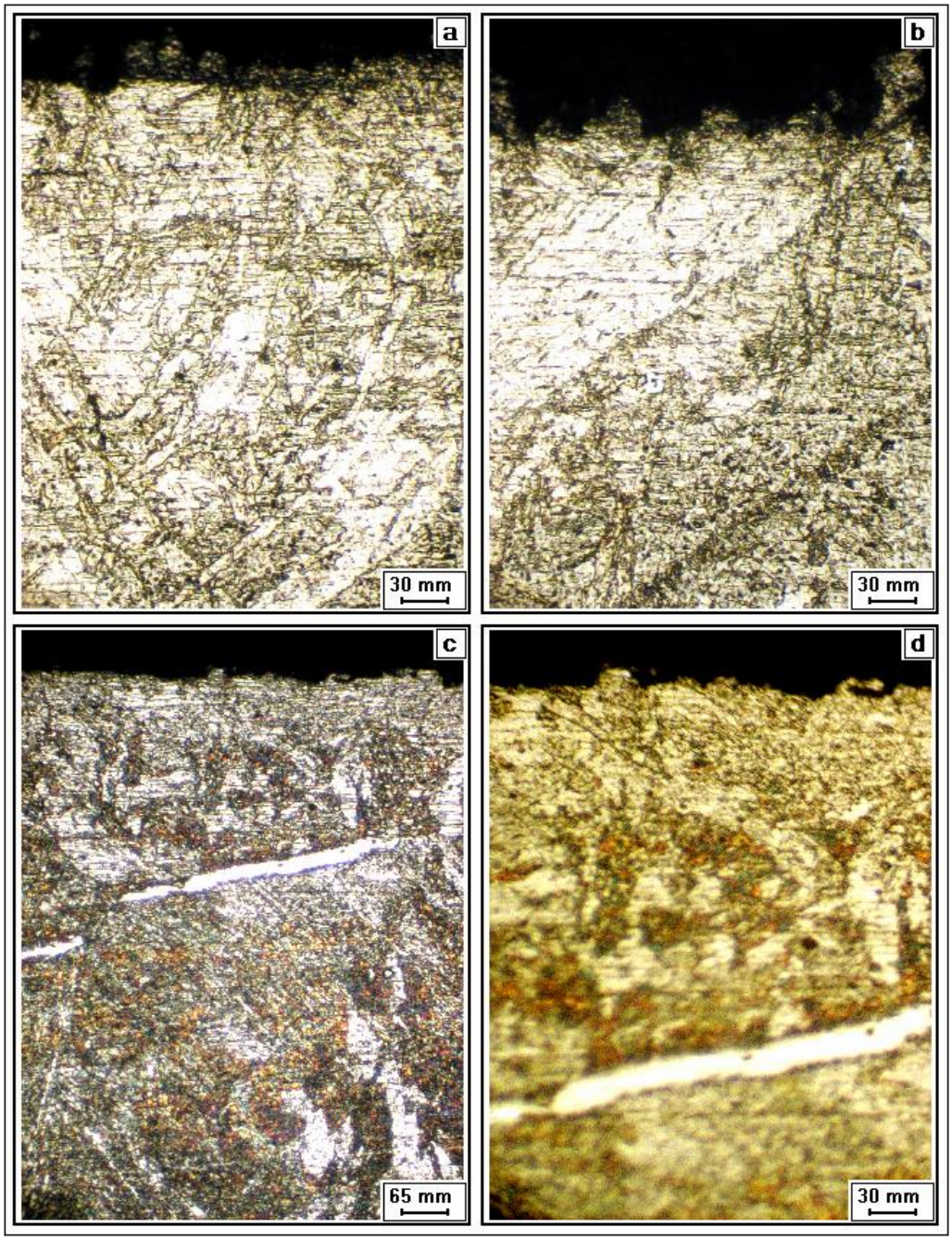

Fig. 2.6.17. Steel microstructure at the specimen top, longitudinal section (analyzed spots are marked by dots in Fig. 2.6.11)

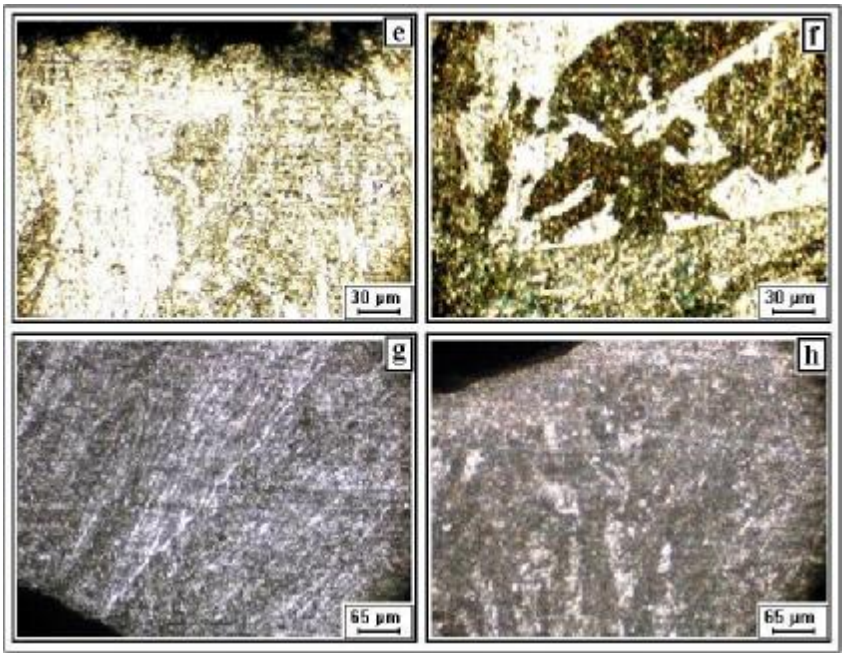

Fig. 2.6.18. Steel microstructure from the specimen top to hole (analyzed spots are marked by dots in Fig. 2.6.11)

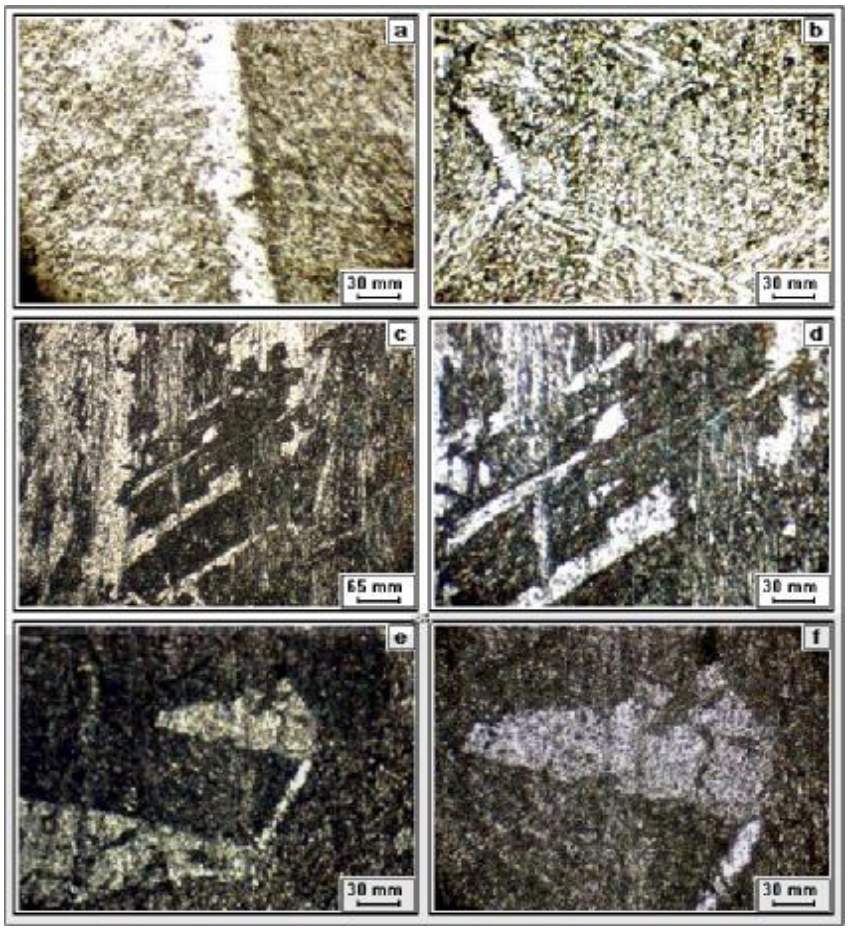

Fig. 2.6.19. Steel microstructure above line 3 and between lines 3 and 4 (Fig. 2.6.11)

3. Discussion of results

1. Four temperature regimes of the interaction of molten C-100 corium and specimen through the crust in inert atmosphere were realized in the test. (see Tab. 3.1)

Table 3.1

Interaction conditions

Maximum steel surface temperature near the specimen axis, C	Heat flux density, average, MW/m^2	Exposure, h	Ablation depth, mm
1075	0.66	5	< 0.006
1180	0.73	11	0.08 ± 0.01
1315	0.81	8.5	0.10 ± 0.01
1435	0.89	9.8	?

The following conclusions can be made from the obtained results:

- At a steel surface temperature of 1075ºC and below, no noticeable melt-vessel steel was observed. That is, under these conditions the crust serves as a reliable protector of the steel specimen from melt attack.
- Iron oxides have been found on the steel surface. At the steel surface temperatures between 1180 and 1315ºC steel oxidation takes place at the expense of the melt and crust oxidizing resources, but since the resources are limited, the process of oxidation approaches saturation.
- During the 4^{th} regime (at 1435ºC on the steel surface), the process of eutectic melting of the subsurface phases started. The first liquid phases (ZrO_2-UO_2-FeO-Fe) formed at approximately 1410ºC at 105,000 sec of the test, which is confirmed by the ultrasonic sensor readings and the collapse of the surface thermocouple TC01. It should be noted that in a different test the temperature of vessel steel melting was found to be 1498ºC by DSC.
- The surface eutectic melting did not disrupt the crust entirety, i.e., the pattern of corium - steel interaction was as follows: melt – crust – liquid sublayer – solid steel.
- The data on the observed process kinetics are not available for the 4^{th} regime, as presently there is no technique for processing anomalous echo signals. The echo signal trend is influenced by the appearance of a liquid phase at the interaction interface.

2. A long-term steel exposure under the high-temperature thermogradient conditions caused changes in the surface layer microstructure to a depth of 10 mm. It was expressed in the grain coarsening and pore formation. A deterioration of mechanical properties of steel may be expected in this layer.

3. The results of SEM/EDX analysis offer a mechanism of high-temperature interaciton of C-100 molten corium with vessel steel through the solid crust under the conditions of “anoxia” (Fig. 3.1).

After the molten pool has formed, the surface of the cooled steel specimen is separated from the melt by a stable crust. As the temperature of the steel surface increases, its oxidation starts. In due course, a FeO sublayer forms on the side of the steel specimen and a Fe_3O_4 sublayer – on the crust side. The solid solution of uranium and zirconium oxides composing the crust loses oxygen and becomes superstoichiometric.

At reaching a certain temperature and components ratio in the region of the formed layers contact, eutectic melting takes place yielding a liquid sublayer.

We believe this temperature to be close to the eutectic temperature of the UO_2 - ZrO_2 - FeO system (CORPHAD project results) and correspond to 1270ºC approximately. At a still higher temperature (roughly 1410ºC), eutectics involving Fe from the steel specimen may form (UO_2 - ZrO_2 – FeO - Fe), and thus the steel specimen melting will be initiated.

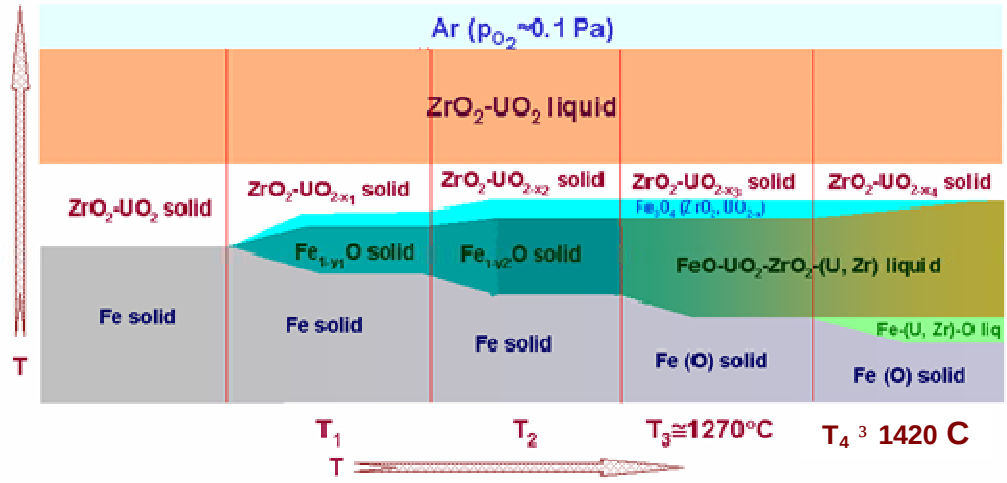

Fig. 3.1 Corium-Steel interaction model

4. The results of the test confirm that the interaction of C-100 corium with vessel steel in inert atmosphere is characterized by a minimum rate in comparison with the test performed at Phase 1 of the Project.

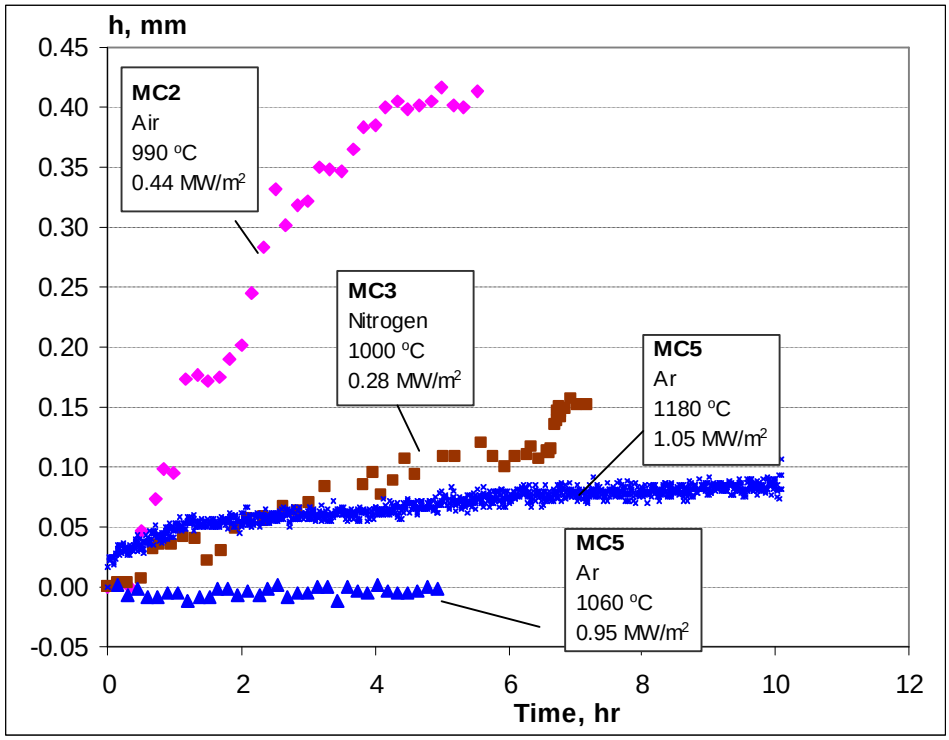

Fig. 3.2 Comparison of steel corrosion rates in MC-2, 3 and 5

Fig. 3.2 demonstrates it well that at comparable values of the temperature on the steel surface and large heat fluxes from corium to the specimen, the rate and depth of steel corrosion with a C-100 corium are considerably smaller than with the corium containing iron oxides.

5. For all the regimes, the temperature conditions of the specimen, distribution of power and Lorentz forces in the molten corium pool and vessel steel specimen have been numerically modelled. The results describe the conditions and characteristic parameters of the specimen/corium melt interaction through the crust. These results may be used in future, for instance, for modelling the molten pool hydrodynamics and, correspondingly, for specifying the distribution of temperatures and heat fluxes at the interface.

4. Conclusions

- The results of the test confirm that the interaction of C-100 corium with vessel steel in inert atmosphere is characterized by a minimum rate in comparison with the test performed at Phase 1 of the Project.
- It was found that liquid phases at the corium/steel interaction interface form at temperatures approximately 90ºC lower than the temperature of steel melting onset.
- The measured kinetics of steel ablation leading to the process saturation may be the consequence of the limited oxidizing resources of corium which are temperature-dependent. It is indirectly confirmed by the absence of significant ablation intensification after liquid phases have formed at the interaction boundary.
- The technique of ultrasonic sounding offers a reliable means of registering kinetics of steel ablation at its surface temperatures not exceeding that of the onset of liquid phases formation. The possibilities of interpreting the echograms obtained at higher temperatures are stull under investigation.

References

1. Workplan for the METCOR, Phase 2 Project.
2. Petrov Yu.B. Induction melting of oxides. L.: Energatomizdat, 1983, 104 p (In Russian).
3. Report on measurements of the vessel steel thermal conductivity. METCOR, Phase 1 Project.
4. Report on the MC-2 test, the METCOR, Phase 1 Project.
5. The technique of U^{+4}, U^{+6} determination with the arsenazo III reagent.
6. Cohen I., Schaner B.E. // J. Nucl. Mater. 1963. Vol. 9. № 1. P. 18-52
7. Romberger K. A., Baes C.F., Stone H.H. // J. Nucl. Mater. 1967. Vol. 29. № 7. PP. 1619-1630
8. Standard technique of steel template grinding and polishing.
9. Gulyayev A.P. Physical metallurgy. M.: Metallurgiya. 1986.